The fine-grained phase-space structure of Cold Dark Matter halos

Mark Vogelsberger[1], Simon D.M. White[1], Amina Helmi[2], Volker Springel[1]

[1] *Max-Planck Institut fuer Astrophysik, Karl-Schwarzschild Strasse 1, D-85748 Garching, Germany* ⋆
[2] *Kapteyn Astronomical Institute, University of Groningen, P.O. Box 800, 9700 AV Groningen, Netherlands* †

ABSTRACT

We present a new and completely general technique for calculating the fine-grained phase-space structure of dark matter throughout the Galactic halo. Our goal is to understand this structure on the scales relevant for direct and indirect detection experiments. Our method is based on evaluating the geodesic deviation equation along the trajectories of individual DM particles. It requires no assumptions about the symmetry or stationarity of the halo formation process. In this paper we study general static potentials which exhibit more complex behaviour than the separable potentials studied previously. For ellipsoidal logarithmic potentials with a core, phase mixing is sensitive to the resonance structure, as indicated by the number of independent orbital frequencies. Regions of chaotic mixing can be identified by the very rapid decrease in the real space density of the associated dark matter streams. We also study the evolution of stream density in ellipsoidal NFW halos with radially varying isopotential shape, showing that if such a model is applied to the Galactic halo, at least 10^5 streams are expected near the Sun. The most novel aspect of our approach is that general non-static systems can be studied through implementation in a cosmological N-body code. Such an implementation allows a robust and accurate evaluation of the enhancements in annihilation radiation due to fine-scale structure such as caustics. We embed the scheme in the current state-of-the-art code GADGET-3 and present tests which demonstrate that N-body discreteness effects can be kept under control in realistic configurations.

Key words: cold dark matter, phase-space structure, dynamics, N-body

1 INTRODUCTION

Dark Matter (DM) is still to be directly detected. The first indirect indications of its existence came in the 1930s, with measurements of the velocities of galaxies in clusters. The cluster mass required to gravitationally bind the galaxies was found to be more than an order of magnitude larger than the sum of the luminous masses of the individual galaxies (Zwicky 1933; Smith 1936). The early detection of large amounts of unseen matter associated with the Local Group (Kahn & Woltjer 1959) was followed in the 1970s by observations of the rotation curves of spiral galaxies which showed that these are flat, or even rising, at distances far beyond their stellar components (Rubin & Ford 1970; Faber & Gallagher 1979; Rubin et al. 1980). Studies of satellite systems suggested that the mass distributions of most galaxies might be an order of magnitude larger and more massive than their visible parts (Ostriker et al. 1974; Einasto et al. 1974). All these discoveries led to the conclusion that a large fraction of mass in the Universe is dark. This has also been supported by recent gravitational lensing studies that demonstrate the existence of extended massive DM halos (e.g. Mandelbaum et al. 2006).

As the dominant mass component of galaxies and large-scale structures, DM has necessarily become a key ingredient in theories of cosmic structure formation. The most successful of these theories is the hierarchical paradigm. In the current version of this model, the DM is composed of nonbaryonic elementary particles known as Cold Dark Matter (CDM) (Peebles 1982). The term "cold" derives from the fact that the DM particles had negligible thermal motions at the time of matter-radiation equality. Their abundance was set when the interaction rate became too small for them to remain in thermal equilibrium with other species in the expanding Universe. The first objects to form in a CDM Universe are small galaxies. They then merge and accrete to give rise to the larger structures we observe today. Thus structure formation occurs in a "bottom-up" fashion (Blumenthal et al. 1984; Davis et al. 1985; Springel et al. 2006).

The crucial test of this paradigm undoubtedly consists in the determination of the nature of DM through direct detection experiments. Among the most promising candidates from the particle physics perspective are axions and neutralinos. Axions were introduced to explain the absence in Nature of strong-CP (Charge conjugation and Parity) violations (Peccei & Quinn 1977). The cosmo-

⋆ {vogelsma,volker,swhite}@mpa-garching.mpg.de
† ahelmi@astro.rug.nl

logical population formed out of equilibrium as a zero momentum Bose condensate. They can be detected through their conversion to photons in the presence of a strong magnetic field, (e.g. Ogawa et al. 1996; Hagmann et al. 1998). Neutralinos are the lightest super-symmetric particles, and may be considered as a particular form of weakly interacting massive particles (WIMPs) (Steigman & Turner 1985). The most important direct detection process for neutralinos is through elastic scattering on nuclei.

Today many experiments are searching for these particles, (Akerib & et al 2004; Sanglard & et al 2005; Schnee 2006; Aprile et al. 2007; Spooner 2007). The main challenge lies in the large background they encounter. Having an idea what the detector signal might look like can help substantially in fine-tuning the experiments in order to increase the chance of a detection. In addition, many experiments are attempting to detect WIMPs indirectly by searching for γ-ray emission from their annihilation (de Boer 2005; de Boer et al. 2005; Bergström & Hooper 2006; Hooper & Serpico 2007). Predictions for this radiation are currently uncertain because very substantial enhancements are possible, at least in principle, from fine-scale structure such as caustics in the dark matter distribution (Dalcanton & Hogan 2001; Mohayaee et al. 2007).

The differential detection rate for WIMPs in a given material (per unit detector mass) is sensitive to the local velocity distribution:

$$\frac{dR}{dQ} = \frac{\rho}{M_\chi} \int d^3v f(\mathbf{v}) v \frac{d\sigma}{dQ} \qquad (1)$$

where Q is the energy deposited in the detector and $d\sigma/dQ$ is the differential cross section for WIMP elastic scattering with the target nucleus. M_χ is the WIMP mass which lies in the GeV to TeV range for currently preferred models. ρ is the local mass density and $f(\mathbf{v})$ the velocity distribution of WIMPs that reach the detector.

From Eq. (1) it is evident that the count rate in a direction-insensitive experiment depends on the velocity distribution of the incident particles and will be modulated by the orbital motion of the Earth around the Sun (Drukier et al. 1986). In most studies, an isotropic Maxwellian distribution relative to the galactic halo has been assumed, (e.g. Freese et al. 1988), although there are other models in the literature, discussing, for example, multivariate Gaussians (Evans et al. 2000). Some attempts at understanding the effect of fine-scale structure in the velocity distribution of DM particles have also been made (Sikivie 1998; Stiff et al. 2001; Hogan 2001).

A significant signal could come from what are known as streams of DM (Sikivie et al. 1995; Helmi et al. 2002; Natarajan & Sikivie 2005). Both axions and WIMPs are cold. In the absence of clustering their present day velocity dispersion would be negligible ($\delta v \sim 10^{-10} c$ for WIMPs and $\delta v \sim 10^{-17} c$ for axions). They are effectively restricted to a 3D hypersurface, a sheet in 6D phase-space. The growth of structure results in continual stretching and folding in phase-space of this initially almost uniform sheet. This process is called mixing. The more strongly the system mixes, the more streams of DM particles are present at a given location in configuration-space. Mixing stretches each sheet and so its density decreases. The existence of distinct streams is a direct consequence of the collisionless character and the coldness of CDM. The situation is sketched in Fig. 1. At the points where the number of streams changes by two, the local configuration-space density of dark matter becomes extremely high. These are caustics of the kind studied by catastrophe theory (Gilmore 1982; Tremaine 1999). Note that Liouville's Theorem prevents the CDM phase-space sheet from ever tearing, although it can be arbitrarily strongly stretched.

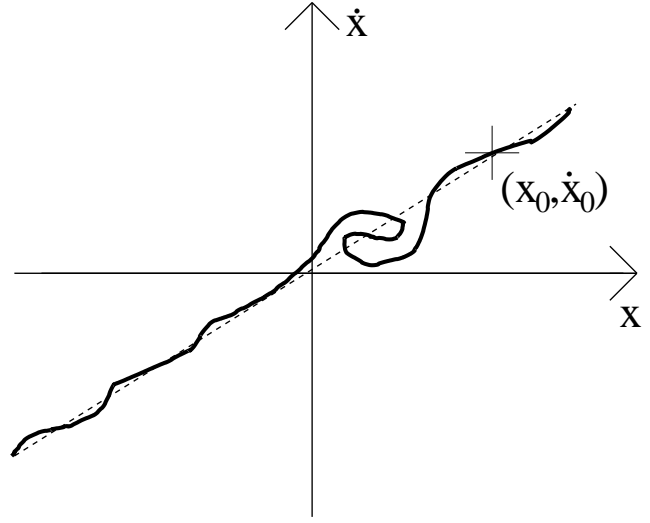If the dark matter density in the solar neighbourhood is dom-

Figure 1. Sketch of an idealised CDM phase-space sheet in the $x, \dot{x}$ plane. The thickness of the line represents the local velocity dispersion within each stream. The small wiggles correspond to initial density perturbations and the multi-valued region reflects the multiple streams created by winding in non-linear regions. Depending on x position an observer sees one or three streams. At points where the number of streams changes by two, a caustic with a very high DM density is present. Such caustics may be significant for the total annihilation flux. The number of streams at each point is a measure of the local amount of mixing. The dashed line represents the Hubble Flow. The cross marks the phase-space coordinates of a particular CDM particle embedded in the flow.

inated by a small number of streams, its velocity distribution will effectively consist of a few discrete values, one for each stream. If, on the other hand, the number of streams is very large, the velocity distribution will be smooth and individual streams will be undetectable. This issue has so far been addressed only under simplified conditions and divorced from its proper cosmological context (Helmi et al. 2002; Natarajan & Sikivie 2005). This is largely because the only tool capable of studying cosmological structure formation in full generality, namely N-body simulations, cannot resolve the relevant scales. For example, Natarajan & Sikivie (2005) estimate that of the order of 10^{12} particles would be required in a simulation of the Milky Way's halo to begin to resolve the streams in the solar neighbourhood. Even the largest simulation so far published, the Via Lactea model (Diemand et al. 2007), is 4 orders of magnitude short of this minimum requirement. It is thus impossible to figure out the number of streams near the Sun and the properties of "typical" streams with current N-body capabilities.

A related issue that has been much discussed is whether caustics can affect direct or indirect detection experiments. Some authors claim that caustics play an important role as stable phenomena connected to any collapsing CDM halo and taking the form of relatively massive rings or shells (Sikivie 1999; Natarajan & Sikivie 2006). Other authors have argued that caustics should be more abundant, weaker and dynamically negligible (Helmi et al. 2002). Even if caustics negligibly affect the gravitational potential, they may have very substantial effects on the annihilation rate of dark matter (Hogan 2001; Bergström et al. 2001; Pieri & Branchini 2005; Mohayaee & Shandarin 2006; Mohayaee et al. 2007; Natarajan 2007). All these papers were able to evaluate the enhancements due to caustics only under restrictive and unrealistic assumptions about symmetry, formation history, etc. While they demonstrate that large enhancement factors may be pos-

sible, they do not provide reliable estimates for the actual enhancement expected. The method we present below is capable of providing such estimates for halos growing as predicted by the ΛCDM model.

In this paper we will present a novel approach that directly analyses structure in the fine-grained phase-space distribution. We circumvent the "number of particle" problem by solving the geodesic deviation equation (GDE) for every DM particle. This allows us to calculate the local properties of the DM stream each simulation particle is embedded in, in particular, its configuration-space density and its local velocity distribution. The mass-weighted number of streams near any point is then the total local density divided by the mean density of the individual local streams. Caustic passages can be detected robustly from the properties of each particle's local stream, and the particle's instantaneous annihilation probability within this stream can be evaluated simply and integrated accurately through caustics.

This paper is the first of a series. Here we introduce our method and apply it to study the evolution of streams in static potentials that are too complex to be analysed using previous techniques. We also implement our scheme in a state-of-the-art N-body simulation code, and use simple test problems to demonstrate that N-body discreteness effects can be kept under control in realistic applications. Later papers will address issues associated with mixing, caustics and annihilation radiation in the full cosmological context.

The outline of our paper is the following: In Section 2 we present a detailed derivation of the GDE and show how it can be used to quantify mixing, to locate caustics, and to calculate stream densities and annihilation rates. Section 3 describes our code, DaMaFlow, which is designed to solve the GDE for single orbits in a wide variety of potentials. In Section 4 we analyse static, separable potentials and compare results from our method to previous work. The fifth section applies our scheme to non-integrable, but still static potentials, revealing their complex phase-space structure. In Section 6 we turn to more realistic non-spherical CDM halo potentials and discuss the influence of halo shape on stream density behaviour. Section 7 discusses the implementation of our method in an N-body code and presents results of simple tests of when discreteness effects compromise studies of stream densities and caustics. The final section summarises our results and gives some conclusions.

2 THE GEODESIC DEVIATION EQUATION

Our scheme for calculating the evolution of the fine-grained phase-space distribution in the neighbourhood of a DM particle is based on the evolution of the distance between two infinitesimally separated particle trajectories. This evolution is described by the Geodesic Deviation Equation (GDE). We use the following notation to clearly distinguish between three- and six-dimensional quantities: an underline denotes a $\mathbb{R}^3$ vector and two of them denote a $\mathbb{R}^{3\times3}$ matrix. An overline denotes a $\mathbb{R}^6$ vector and two of them denote a $\mathbb{R}^{6\times6}$ matrix. Thus a general phase-space vector is composed of two three-dimensional vectors: $\overline{x} = (\underline{x}, \underline{v})$.

To derive the GDE we first write down the equations of motion for a DM particle. These are simply

$$\underline{\ddot{x}}\left(t; \underline{x}_0, \underline{v}_0\right) = -\underline{\nabla}_x \Phi\left(\underline{x}\left(t; \underline{x}_0, \underline{v}_0\right)\right), \qquad (2)$$

with initial conditions $\underline{x}\left(t_0; \underline{x}_0, \underline{v}_0\right) = \underline{x}_0 \quad \underline{v}\left(t_0; \underline{x}_0, \underline{v}_0\right) = \underline{v}_0$.

As $\underline{\dot{x}} = \underline{v}$ the equation of motion in phase-space can be written:

$$\dot{\overline{x}}\left(t; \overline{x}_0\right) = \left(\begin{array}{c} \underline{v} \\ -\underline{\nabla}_x \Phi\left(\underline{x}\left(t; \overline{x}_0\right)\right) \end{array} \right) = \overline{\Psi}\left(\overline{x}\left(t; \overline{x}_0\right)\right), \quad (3)$$

with initial conditions $\overline{x}\left(t_0; \overline{x}_0\right) = \overline{x}_0 = (\underline{x}_0, \underline{v}_0)$.

We want to calculate the local stream density around the DM particle whose trajectory in phase-space is given by $\overline{x}\left(t; \overline{x}_0\right)$. To do so, we first ask how the displacement vector to a neighbouring DM particle in phase-space evolves with time:

$$\overline{\delta}\left(t\right) = \overline{x}\left(t; \overline{x}_0 + \overline{\delta}_0\right) - \overline{x}\left(t; \overline{x}_0\right). \qquad (4)$$

Note that $\overline{\delta}\left(t\right)$ is the displacement between the reference DM particle, which was at $\overline{x}_0$ at time t_0, and another particle which was at $\overline{x}_0 + \overline{\delta}_0$ at t_0. We are interested in properties in the immediate neighbourhood of the reference particle, so $\overline{\delta}_0$ is an infinitesimal displacement. This allows us to work to linear order:

$$\overline{\delta}\left(t\right) \cong \left(\overline{\delta}_0 \cdot \overline{\nabla}_{x_0}\right) \overline{x}\left(t; \overline{x}_0\right). \qquad (5)$$

Introducing the phase-space distortion tensor $\overline{\overline{D}}$ (note that this is a 6×6 tensor)

$$\overline{\overline{D}}\left(t; \overline{x}_0\right) \equiv \frac{\partial \overline{x}}{\partial \overline{x}_0}\left(t; \overline{x}_0\right), \qquad (6)$$

we can rewrite Eq. (5) as a simple linear transformation from the starting phase-space displacement $\overline{\delta}_0$ to the displacement $\overline{\delta}(t)$ at time t:

$$\overline{\delta}\left(t\right) \cong \overline{\overline{D}}\left(t; \overline{x}_0\right) \overline{\delta}_0. \qquad (7)$$

Because $\overline{\delta}_0$ is an arbitrary displacement vector, the distortion tensor describes how the complete local phase-space neighbourhood around the reference DM particle gets distorted while it is orbiting in the given potential. The time evolution of $\overline{\delta}(t)$ follows from the time evolution of the two trajectories. Again we can work this out in linear order[1]:

$$
\begin{aligned}
\dot{\overline{\overline{D}}}\left(t; \overline{x}_0\right) \overline{\delta}_0 &\cong \dot{\overline{\delta}}\left(t\right) \\
&= \overline{\Psi}\left(\overline{x}\left(t; \overline{x}_0\right) + \overline{\delta}\left(t\right)\right) - \overline{\Psi}\left(\overline{x}\left(t; \overline{x}_0\right)\right) \\
&\cong \left(\overline{\delta}\left(t\right) \cdot \overline{\nabla}_x\right) \overline{\Psi}\left(\overline{x}\left(t; \overline{x}_0\right)\right) \\
&\cong \left(\left(\overline{\overline{D}}\left(t; \overline{x}_0\right) \overline{\delta}_0\right) \cdot \overline{\nabla}_x\right) \overline{\Psi}\left(\overline{x}\left(t; \overline{x}_0\right)\right). \qquad (8)
\end{aligned}
$$

To derive the equation of motion for the distortion tensor itself we evaluate Eq. (8) for six unit vector phase-space displacements $\overline{\delta}_0^{(j)}$ with $\delta_{0,\alpha}^{(j)} = \delta_{\alpha j}$ where $\alpha, j = 1, 2, \ldots, 6$, and δ_{ab} is the Kronecker delta. Taking into account Einstein's sum convention this yields for each component of Eq. (8)

$$
\begin{aligned}
\dot{D}_{ij}\left(t; \overline{x}_0\right) &= \dot{D}_{i\alpha}\left(t; \overline{x}_0\right) \delta_{0,\alpha}^{(j)} \\
&\cong \left(D_{\beta\gamma}\left(t; \overline{x}_0\right) \delta_{0,\gamma}^{(j)} \frac{\partial}{\partial x_\beta}\right) \Psi_i\left(\overline{x}\left(t; \overline{x}_0\right)\right) \\
&= \left(D_{\beta\gamma}\left(t; \overline{x}_0\right) \delta_{\gamma j} \frac{\partial}{\partial x_\beta}\right) \Psi_i\left(\overline{x}\left(t; \overline{x}_0\right)\right) \\
&= \left(D_{\beta j}\left(t; \overline{x}_0\right) \frac{\partial}{\partial x_\beta}\right) \Psi_i\left(\overline{x}\left(t; \overline{x}_0\right)\right) \\
&= T_{i\beta}\left(t; \overline{x}_0\right) D_{\beta j}\left(t; \overline{x}_0\right), \qquad (9)
\end{aligned}
$$

---

[1] As $\overline{\delta}_0$ can be chosen arbitrarily small, this is always possible.

where we have introduced the phase-space tidal tensor

$$\overline{\overline{T}}(t;\overline{x}_0) = \begin{pmatrix} \underline{0} & \underline{1} \\ \underline{\underline{T}}(t;\underline{x}_0) & \underline{0} \end{pmatrix},$$ (10)

and $\underline{T}$ is the configuration-space tidal tensor given by the second derivatives of the gravitational potential $T_{ij} = -\partial^2\Phi/\partial x_i \partial x_j$. As we are are only interested in linear order we replace $\cong$ by $=$ in Eq. (9) and get an equation of motion for the 6D distortion tensor:

$$\dot{\overline{\overline{D}}}(t;\overline{x}_0) = \overline{\overline{T}}(t;\overline{x}_0)\,\overline{\overline{D}}(t;\overline{x}_0).$$ (11)

Note that this first-order tensor differential equation represents a system of 36 coupled ordinary first-order differential equations. To solve them we need to specify initial conditions. These follow from the constraint

$$\overline{\delta}_0 = \overline{\overline{D}}(t_0;\overline{x}_0)\,\overline{\delta}_0 \quad\Rightarrow\quad \overline{\overline{D}}(t_0;\overline{x}_0) = \overline{\overline{1}}.$$ (12)

DM behaves like a collisionless fluid and its fine-grained phase-space density $f(\overline{x},t)$ is described by the well-known Vlasov equation:

$$\frac{\partial f}{\partial t} + \underline{v}\cdot\underline{\nabla}_x f - \underline{\nabla}_x\Phi\cdot\underline{\nabla}_v f = 0,$$ (13)

Using the Lagrangian derivative this reads $\mathrm{D}f/\mathrm{D}t = 0$, meaning that the local fine-grained phase-space density has to be conserved along the orbit of every particle in the system. Imagine N particles that fill a small phase-space volume $\mathrm{d}V_0 = \mathrm{d}\underline{x}_0\mathrm{d}\underline{v}_0$ around the DM reference particle at time t_0. At a later time t these particles fill a volume $\mathrm{d}V = \mathrm{d}\underline{x}\mathrm{d}\underline{v}$ around the reference particle at $\overline{x}(t;\overline{x}_0)$. Conservation of phase-space density implies that the two volumes are the same $\mathrm{d}V_0 = \mathrm{d}V$. The evolution of the initial displacement vectors $\overline{\delta}_0^{(n)}$ from the reference particle to one of the N other particles in the volume is described by the distortion tensor associated with the reference particle:

$$\overline{\delta}^{(n)}(t) = \overline{\overline{D}}(t;\overline{x}_0)\,\overline{\delta}_0^{(n)} \qquad n = 1, 2, \ldots, N$$ (14)

The change in volume due to this linear transformation is given by the determinant $\det(\overline{\overline{D}}(t;\overline{x}_0))$. As this volume has to be conserved, the determinant of the phase-space distortion tensor has to be conserved. Note that not only must the volume be conserved, but also the orientation of the volume element. This means that the sign of the determinant is also fixed. From the initial conditions Eq. (12) one gets $\det(\overline{\overline{D}}(t;\overline{x}_0))=1$ at all times. This fact can be used to check numerical solutions of the equations.

The structure of Eq. (11) allows the equations of motion for the distortion to be broken down to a set of equations that is more convenient to work with. Let us first rewrite Eq. (11) using blocks of 3×3 tensors:[2]

$$\frac{\mathrm{d}}{\mathrm{d}t}\begin{pmatrix} \underline{\underline{D}}_{xx} & \underline{\underline{D}}_{xv} \\ \underline{\underline{D}}_{vx} & \underline{\underline{D}}_{vv} \end{pmatrix} = \begin{pmatrix} \underline{0} & \underline{1} \\ \underline{\underline{T}} & \underline{0} \end{pmatrix}\begin{pmatrix} \underline{\underline{D}}_{xv} & \underline{\underline{D}}_{xv} \\ \underline{\underline{D}}_{vx} & \underline{\underline{D}}_{vv} \end{pmatrix}$$
$$= \begin{pmatrix} \underline{\underline{D}}_{vx} & \underline{\underline{D}}_{vv} \\ \underline{\underline{T}}\,\underline{\underline{D}}_{xx} & \underline{\underline{T}}\,\underline{\underline{D}}_{xv} \end{pmatrix}.$$

Writing down the equation for each matrix block yields four equations:

$$\dot{\underline{\underline{D}}}_{xx} = \underline{\underline{D}}_{vx} \qquad ; \qquad \dot{\underline{\underline{D}}}_{xv} = \underline{\underline{D}}_{vv},$$ (15)

and

$$\dot{\underline{\underline{D}}}_{vx} = \underline{\underline{T}}\,\underline{\underline{D}}_{xx} \qquad ; \qquad \dot{\underline{\underline{D}}}_{vv} = \underline{\underline{T}}\,\underline{\underline{D}}_{xv}.$$ (16)

These can be combined to give:

$$\ddot{\underline{\underline{D}}}_{xx} = \underline{\underline{T}}\,\underline{\underline{D}}_{xx} \qquad ; \qquad \ddot{\underline{\underline{D}}}_{xv} = \underline{\underline{T}}\,\underline{\underline{D}}_{xv}.$$ (17)

Thus we get two identical differential equations of second-order for two 3×3 tensors whose dynamics is driven by the ordinary tidal tensor. From the initial condition for the 6D distortion one can see that the only difference between $\underline{\underline{D}}_{xx}$ and $\underline{\underline{D}}_{xv}$ lies in the appropriate initial conditions: $\underline{\underline{D}}_{xx}(t_0;\underline{x}_0) = \underline{1}$, $\dot{\underline{\underline{D}}}_{xx}(t_0;\underline{x}_0) = \underline{0}$ and $\underline{\underline{D}}_{xv}(t_0;\underline{x}_0) = \underline{0}$, $\dot{\underline{\underline{D}}}_{xv}(t_0;\underline{x}_0) = \underline{1}$ in the two cases. From the solutions of these two initial condition problems the 6D distortion solution can then be constructed:

$$\overline{\overline{D}} = \begin{pmatrix} \underline{\underline{D}}_{xx} & \underline{\underline{D}}_{xv} \\ \mathrm{d}/\mathrm{d}t\underline{\underline{D}}_{xx} & \mathrm{d}/\mathrm{d}t\underline{\underline{D}}_{xv} \end{pmatrix}.$$ (18)

Up to this point we have worked out all equations in phase-space. As we are interested in the stream density in configuration-space, we need to project down to this space. As already mentioned, CDM lies on a thin sheet in phase-space. This sheet has a certain orientation at the starting point of the reference DM particle. Take $(\underline{x},\underline{v}) : \underline{v} = \underline{V}(\underline{x};t_0,\overline{x}_0)$ to be the local parametrisation of the sheet surrounding this particle at time t_0[3]. Now we ask how an infinitesimal displacement $\underline{\delta}_{0,x}$ in configuration-space is distorted by evolution. First we note that any displacement in $\underline{x}$ implies a displacement in velocity-space due to the restriction of particles to the sheet:

$$\underline{\delta}_{0,v} = \underline{\underline{V}}_x(\overline{x}_0)\,\underline{\delta}_{0,x} \quad ; \quad \underline{\underline{V}}_x(\overline{x}_0) = \frac{\partial \underline{V}}{\partial \underline{x}}(\underline{x}_0;t_0,\overline{x}_0).$$ (19)

The phase-space distortion $\overline{\overline{D}}$ describes how the corresponding phase-space displacement $(\underline{\delta}_{0,x},\underline{\delta}_{0,v})$ evolves. We are here interested in the configuration-space part of the phase-space displacement at time t:

$$\underline{\delta}_x(t) = \underline{\underline{D}}_{xx}(t;\overline{x}_0)\,\underline{\delta}_{0,x} + \underline{\underline{D}}_{xv}(t;\overline{x}_0)\,\underline{\underline{V}}_x(\overline{x}_0)\,\underline{\delta}_{0,x}.$$ (20)

The evolution of the displacement in configuration-space can also be described by a linear transformation:

$$\underline{\delta}_x(t) = \underline{\underline{D}}(t;\overline{x}_0)\,\underline{\delta}_{0,x},$$

where we have introduced the configuration-space distortion tensor (note that this is a 3×3 tensor)

$$\underline{\underline{D}}(t;\overline{x}_0) = \underline{\underline{D}}_{xx}(t;\overline{x}_0) + \underline{\underline{D}}_{xv}(t;\overline{x}_0)\,\underline{\underline{V}}_x(\overline{x}_0).$$ (21)

This tensor can also be derived with the help of two projection operators:

$$\underline{\underline{D}}(t;\overline{x}_0) = \begin{pmatrix} \underline{1} & \underline{0} \end{pmatrix}\overline{\overline{D}}(t;\overline{x}_0)\begin{pmatrix} \underline{1} \\ \underline{\underline{V}}_x(\overline{x}_0) \end{pmatrix}.$$ (22)

As in the case of phase-space distortion, the change in volume due to the linear transformation in Eq. (21) is given by the determinant,

---

[2] We suppress the argument $t;\overline{x}_0$ to avoid confusion.

[3] Such a parametrisation is always possible locally, but due to mixing there is, in general, no simple global parametrisation of the stream. This is only possible for very early times, where the sheet is dominated by the Hubble Flow, the $\underline{x} - \underline{v}$ relation is one-to-one, and the stream density is almost uniform.
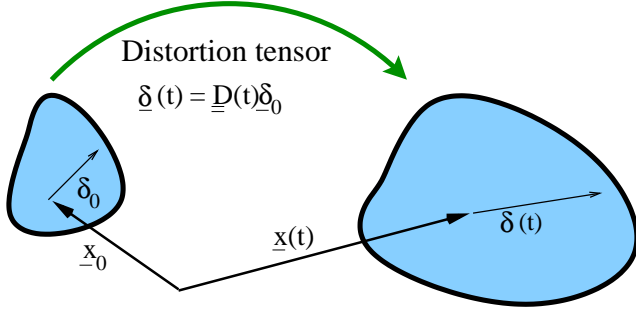
Figure 2. The configuration-space distortion tensor $\underline{\underline{D}}$ describes how an initial small configuration-space displacement $\underline{\delta}_0$ evolves in time. This reflects the stretching of an infinitesimally small cloud of virtual particles around the reference particle that is placed at $\underline{x}_0$ at time t_0. The stretching of the cloud is driven by the tidal field that the DM particle encounters as it orbits.

so that the stream density in configuration-space is proportional to the inverse of this determinant:

$$\rho_{\mathrm{stream}}(t) \propto \frac{1}{\left| \det\left(\underline{\underline{D}}(t; \overline{x}_0) \right) \right|}. \tag{23}$$

At time t_0 the configuration-space distortion tensor equals unity. Thus, if we norm the stream density to its initial value, we get the following relation for the normed stream density:

$$\rho_{\mathrm{stream}}^{\mathrm{normed}}(t) = \frac{1}{\left| \det\left(\underline{\underline{D}}(t; \overline{x}_0) \right) \right|}. \tag{24}$$

In the rest of this paper we will almost always discuss this normed stream density.

In Fig. 2 we sketch the distortion of the infinitesimal cloud around the reference DM particle. Note the difference between the stream density evolution in configuration-space and in phase-space. The volume of the small cloud grows in Fig. 2 and is not constant anymore! This is a result of the projection from phase-space to configuration-space. Nearby trajectories spatially diverge in time.

This formalism can be used to identify caustics in a very efficient way. If the DM particle passes through a caustic $\det(\underline{\underline{D}})$ passes through zero, and the stream density goes to infinity (for perfectly cold DM). A small cloud surrounding the reference particle turns inside out as it passes through the caustic. This corresponds to a change in sign of the determinant, and thus can easily identified numerically. This property allows the location of caustics to be mapped accurately even in complex configurations. Note that the possibility of sign changes explains why we took the modulus of the determinant in Eq. (23).

The complex fine-grained phase-space structure and especially the caustics expected in CDM halos are likely to substantially enhance annihilation radiation. These effects have so far been analysed only under quite simplified conditions (Hogan 2001; Bergström et al. 2001; Pieri & Branchini 2005; Mohayaee & Shandarin 2006; Mohayaee et al. 2007; Natarajan 2007). As a result, it is unclear how strong such enhancement effects will be in the proper cosmological context. Previous studies of annihilation radiation from N-body halos had realistic formation histories but were unable to resolve caustics. They estimated emissivities from the local mean CDM density, thus effectively excluding contributions from single streams (Stoehr et al. 2003; Diemand et al. 2007). Hogan (2001) noted that this results in an underestimation of the annihilation rate, and suggested that anni-

hilation might, in fact, be dominated by contributions from the neglected caustics (which he baptised as "micropancakes").

Our formalism enables a robust and accurate calculation of the contribution to the annihilation radiation from individual streams. The annihilation rate for each particle due to encounters with other particles in its own stream can be evaluated directly from the local stream velocity distribution and density. Integrating these rates along the trajectories of all particles produces a Monte Carlo estimate of the intrastream annihilation rate for the system as a whole. This automatically includes the contributions from all caustics and is exactly the fine-scale contribution which is missing from standard N-body-based estimates of annihilation luminosities.

We now discuss briefly how this is done. Given the very small primordial velocity dispersion σ_0 of CDM, and approximating the initial configuration-space density as a constant ρ_0 we can write the phase-space density around a reference particle at the initial time t_0 as follows: [4]

$$f(\overline{x}, t_0) = \rho_0 N_0 \exp(-\frac{1}{2}(\overline{x} - \overline{x}(t_0; \overline{x}_0))^{\dagger} \overline{\overline{W}}_0 (\overline{x} - \overline{x}(t_0; \overline{x}_0))),$$

where

$$\overline{\overline{W}}_0 = \sigma_0^{-2} \mathrm{diag}(\underline{0},\ \underline{1}),$$

and $N_0 = (2\pi)^{-3/2} \sigma_0^{-3}$. Note that this represents a Gaussian distribution in velocity-space and a constant density in configuration-space.

Using $\overline{\delta}(t) = \overline{\overline{D}}(t) \overline{\delta}_0$ we obtain the phase-space density around the particle at the later time t:

$$f(\overline{x}, t) = \rho_0 N_0 \exp(-\frac{1}{2}(\overline{x} - \overline{x}(t; \overline{x}_0))^{\dagger} \overline{\overline{W}}(t)(\overline{x} - \overline{x}(t; \overline{x}_0))),$$

where

$$\overline{\overline{W}}(t) = \left(\overline{\overline{D}}(t)^{-1} \right)^{\dagger} \overline{\overline{W}}_0 \left(\overline{\overline{D}}(t)^{-1} \right).$$

The configuration-space density around the reference particle at $\underline{x}(t; \overline{x}_0)$ is simply the integral of the phase-space density over all velocities evaluated at $\underline{x}(t; \overline{x}_0)$:

$$\rho(t) = \rho_0 \frac{\sigma_1(t)\sigma_2(t)\sigma_3(t)}{\sigma_0^3}, \tag{25}$$

where the velocity dispersions $\sigma_i(t)$ are given by $1/\sqrt{\lambda_i(t)}$ and $\lambda_i(t)$ are the eigenvalues of the velocity submatrix of $\overline{\overline{W}}(t)$. The velocity distribution in the principal axis frame of the velocity ellipsoid centred on the particle's position and velocity is given by:

$$g(\underline{v}) = N(t) \exp(-\frac{1}{2}\underline{v}^{\dagger} \mathrm{diag}\left(\sigma_1(t),\ \sigma_2(t),\ \sigma_3(t)\right)^{-2} \underline{v}),$$

where $N(t) = 1/((2\pi)^{3/2}\sigma_1(t)\sigma_2(t)\sigma_3(t))$. Note that this velocity distribution is normalised, i.e. its integral over velocity space is unity.

These quantities allow us to calculate the instantaneous annihilation rate at each point on the particle's trajectory:

$$\frac{\mathrm{d}A}{\mathrm{d}t} = \frac{\rho(t)}{m} \int \mathrm{d}^3 v\, \sigma_A(v) v g(\underline{v}) = \frac{\rho(t)\langle \sigma_A v \rangle}{m} \tag{26}$$

where m is the particle mass and $\sigma_A(v)$ the annihilation cross-section. We note that in many WIMP models the annihilation cross-section is inversely proportional to encounter velocity, and in this case $\langle \sigma_A v \rangle$ is independent of the actual local velocity distribution

---

[4] † denotes the transpose of a matrix

(Jungman et al. 1996). An image of the system in annihilation radiation can be constructed by integrating all particles forward over a short time interval and summing their annihilation contributions into a pixel array. We note that equation (26) exhibits near-singular behaviour as particles pass through caustics and as a result special care is needed to obtain the correct contribution to the annihilation luminosity in this situation. This will be discussed more fully in later papers.

3   THE DAMAFLOW CODE

We have developed the code DaMaFlow to test our GDE scheme by analysing the behaviour of streams in a broad range of static potentials. DaMaFlow integrates the equations of motion and in parallel the GDE for a single orbit within user-specified potentials. This requires solving $3 + 18$ second-order differential equations in parallel. The integration algorithm can be chosen to be a symplectic second-order leapfrog (Drift-Kick-Drift or Kick-Drift-Kick formulation) or alternatively the energy-conserving and adaptive Dop853 algorithm (Hairer et al. 1993) of order 8 that allows dense output and is very fast. Studies focusing on complex phase-space structures, especially in the field of chaos analysis, often use the Dop853 algorithm (or even higher order schemes) because of its high precision. On the other hand N-body codes often implement the leapfrog method because it is the best compromise between performance and accuracy. We find that with a moderate fixed time-step, both formulations of leapfrog are able to give comparable results to Dop853. This is an important point because it is not possible to run N-body simulations with slow but accurate high-order ODE solvers like Dop853.

DaMaFlow is also set up to do a Numerical Analysis of Fundamental Frequencies (NAFF) (Laskar 1988, 1990; Papaphilippou & Laskar 1996; Laskar 2003) and of the resonances associated with the chosen orbit. The fundamental frequencies are revealed by an integer programming routine. This is needed so that we can study the relation between the existence of well-defined fundamental frequencies or resonances and stream density behaviour. The NAFF method determines a quasi-periodic approximation to the orbital motion. For ordinary Fast-Fourier-Transforms (FFT) the accuracy of the determination of the frequencies is of the order of $1/T$, where T is the sampling interval. The NAFF method has an accuracy of $1/T^4$. Thus it makes spectral analysis a lot faster compared to classical Fourier techniques, for example, those used in Binney & Spergel (1982).

To scan large parts of phase-space, DaMaFlow can be run in parallel on batch systems in order to integrate a large number of different orbits simultaneously. A fast automated stream density fitting routine was built in to facilitate efficient analysis of the underlying phase-space without user interaction. Before this fitting can be done, the stream density has to be smoothed to remove the large density spikes produced by caustics. DaMaFlow does this by extracting and fitting the lower envelope of the stream density time series. This envelope is constructed while the orbit integration is running by an iterative on-the-fly minimum finder.

From a numerical point of view, solving the GDE is quite difficult in chaotic regions of phase-space. In these regions the infinitesimal phase-space volume around the reference particle gets distorted very strongly. This produces large numerical values in the phase-space distortion tensor. And this can lead to overflows and round-off errors in numerical computations. In chaos analysis it is an established method to do some kind of re-norming to suppress

these problems. We can do something similar to follow the evolution of phase-space density evolution. We use the transitivity of the phase-space distortion tensor:

$$\overline{\overline{D}}_{t_1 \to t_3} = \overline{\overline{D}}_{t_2 \to t_3} \quad \overline{\overline{D}}_{t_1 \to t_2} \tag{27}$$

where $\overline{\overline{D}}_{t_i \to t_j}$ with $i < j$ is the solution of the GDE with $\overline{\overline{D}}_{t_i \to t_j}(t_i) = \overline{\overline{1}}$ evaluated at time t_j. So the phase-space volume can be written as:

$$\det\left(\overline{\overline{D}}_{t_1 \to t_3}\right) = \det\left(\overline{\overline{D}}_{t_2 \to t_3}\right) \quad \det\left(\overline{\overline{D}}_{t_1 \to t_2}\right) \tag{28}$$

Thus dividing the time integration interval and re-initialising the distortion after each interval avoids large numerical values. This is very similar to the re-norming techniques used for calculating the largest Lyapunov exponents of chaotic systems, where the re-norming frequency is chosen to be of the order of the dynamical time-scale (Lichtenberg & Lieberman 1983; El-Zant 2002). Although this approach works nicely for such applications, it does not help us when calculating the stream density evolution, because we need the entire phase-space distortion information from initial to final time. It is not possible to separate the configuration-space part of the phase-space distortion and to do a similar re-norming. Thus one cannot avoid large numbers during the calculation. DaMaFlow therefore calculates all quantities in double-precision (64 bits=8 bytes). Even in chaotic regions this is enough to follow the system for a substantial amount of time. We note that the phase-space density calculation involves the determinant of a 6×6 matrix, whereas the stream density only involves the determinant of a 3×3 matrix. As a result stream density calculations are less strongly affected by large numbers and overflows. We note that special software libraries can provide even higher precision (e.g. the GMP library [5]).

Since we wish to implement the GDE formalism also into an N-body code, execution speed and memory consumption are important considerations. For each particle we need to store the full 6D phase-space distortion tensor and the particle's tidal tensor. This results in $36 + 6$ extra numbers per particle. Thus a 500^3 particle simulation in double-precision needs already about 39 Gbytes of random access memory (RAM) just for the GDE calculation, assuming we store all information for every particle.

4   INTEGRABLE POTENTIALS

Before presenting some results for the evolution of stream densities in integrable potentials we want briefly to discuss the choice of the initial sheet orientation that goes into $\underline{\underline{V}}_x(\overline{x}_0)$ in equation (19). This depends, of course, on the starting time t_0 and the problem that is to be studied. For example, in a cosmological context $\underline{\underline{V}}_x(\overline{x}_0)$ is given by the linear initial conditions, so by the coupled initial density and velocity fields. We note that, to zeroth order, the sheet orientation is simply given by the Hubble Flow: $\underline{v}(\underline{x}_0, t_0) = H(t_0)\underline{x}_0$.

What is the impact of the initial orientation on later evolution? In Fig. 3 we show the evolution of the normed stream density, as calculated from eq. (24), for a single orbit with four different choices of initial stream orientation. For this test we have used a spherical Hernquist potential:
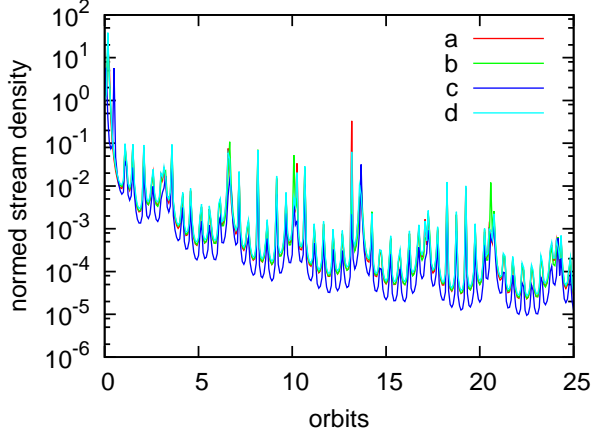
$$\Phi(r) = -\frac{GM}{r+a}, \tag{29}$$

---

[5] http://www.gmplib.org

Figure 3. Stream density evolution for different initial sheet orientations $\underline{\underline{V}}_x(\overline{x}_0)$ in a static Hernquist potential. The general shape of the four curves is very similar. The long-term behaviour does not in general depend on the initial sheet orientation.

with $M = 1.86 \times 10^{12} M_\odot$ and $a = 34.5$ kpc. The reference particle begins its orbit with $\underline{x}_0 = (35, 17.6, 4)$ kpc and $\underline{v}_0 = (-316.9, -16.3, -4)$ km s^{-1}. The initial sheet orientations were chosen to be (in units of km s^{-1} kpc^{-1}): $a : \underline{0}$, $b : \underline{\underline{1}}$,

$$c : \begin{pmatrix} 1 & 10 & 0 \\ 10 & 1 & 0 \\ 0 & 0 & 1 \end{pmatrix} \quad \text{and} \quad d : \begin{pmatrix} 1 & 1 & -2 \\ -1 & 1 & -1 \\ 2 & -1 & 1 \end{pmatrix}.$$

It is striking that all four curves have very similar shape and very similar caustic spacings, although the caustic locations vary. The long-term behaviour does not depend on initial sheet orientation, at least in this case. Orientation c produces lower densities than the others because the scale of $\underline{\underline{V}}_x(\overline{x}_0)$ is larger, but the shape of the lower envelope is very similar.

Natarajan & Sikivie (2006) show that the caustic shape in configuration-space is, in general, affected by the relative size of the $\underline{\underline{V}}_x(\overline{x}_0)$ matrix elements. A detailed analysis of caustic shape thus requires choosing $\underline{\underline{V}}_x(\overline{x}_0)$. For example, in their model for the Milky Way halo Natarajan & Sikivie (2006) initialised trajectories at the turnaround sphere with a $\underline{\underline{V}}_x(\overline{x}_0)$ loosely motivated by tidal torque theory. This restricted the form and scale of the matrix, but still left a lot of freedom. Here our main motivation is not to analyse caustic shapes, but rather the long-term behaviour of the fine-grained phase-space distribution, in particular of stream densities. The initial sheet orientation is thus not an important issue for us. In the following we will consider quite general orbits, but will arbitrarily set $\underline{\underline{V}}_x(\overline{x}_0) = \underline{0}$ unless otherwise stated [6]. Note that the choice of $\underline{\underline{V}}_x(\overline{x}_0)$ does not influence the dynamical evolution of the distortion tensor as it is not part of the initial conditions for the GDE. Only the final projection to configuration-space is affected by initial sheet orientation.

From a dynamical point of view, static, integrable potentials are very simple. The motion within them can be described in terms of action/angle variables and their Hamiltonian can be expressed solely as a function of the actions $H = H(\mathbf{J})$. All motion in these

potentials is regular, so there are no chaotic regions in their phase-space. In action-angle space the orbits lie on tori and are characterised by a fixed number of fundamental frequencies. DM particles in integrable potentials will experience only phase mixing.

Because of these simple properties Helmi & White (1999), hereafter HW, were able to develop an analytic linearised treatment based on action-angle variables to derive results for the stream density behaviour. In their paper they did not specifically focus on CDM, but rather analysed how Gaussian clouds in action-angle space evolve with time.

As an example of an integrable potential, we apply our method to several Eddington potentials $\Phi(r, \theta) = \Phi_1(r) + \eta(\beta \cos \theta)/r^2$ (Lynden-Bell 1962). These are separable in spherical coordinates. The third integral for this type of potential is $I_3 = \frac{1}{2}L^2 + \eta(\beta \cos \theta)$. We chose the following example of an Eddington potential,

$$\Phi(r, \theta) = v_h^2 \log\left(r^2 + d^2\right) + \frac{\beta^2 \cos^2 \theta}{r^2}, \tag{30}$$

with $v_h = 1$ km s^{-1}, $d = 1$ kpc, $\beta = 2.5$ kpc km s^{-1} [7], and studied an orbit which starts at $\underline{x}_0 = (5, 3, 2)$ kpc with a velocity of $\underline{v}_0 = (0.62, 0.62, 0.104)$ km s^{-1}.

In Fig. 4 we show the evolution of the stream density for this orbit, i.e. the projection from phase-space to configuration-space for an initial condition with $\underline{\underline{V}}_x(\overline{x}_0) = \underline{0}$. Here and elsewhere (unless otherwise stated) we define 'the 'orbital period'' as the radial oscillation period for the purpose of making such plots. The late-time behaviour of the stream density can be fitted by an analytic formula derived by HW:

$$\rho(\underline{x}, t) = A \frac{1}{r^2 \sin \theta |p_r p_\theta|} \frac{1}{(t/t_{\text{orbital}})^3}, \tag{31}$$

with only one fitting parameter A. Comparing this to the result for the long-term behaviour in HW (Eq. 37) it is clear that A just reflects the initial phase-space distribution and the orbital parameters (the derivatives of the fundamental frequencies with respect to the actions). The results in HW are calculated for a Gaussian cloud in phase-space, not a cold sheet as in our case. Since the initial distribution only affects A, the long-term behaviour of the two configurations is the same, as shown in Fig. 4.

One can clearly see that our method produces caustics at the correct positions and is also able to recover the secular evolution of the stream density, the $1/(t/t_{\text{orbital}})^3$ density decrease. We note also the initial quasi-exponential stream density decrease that is often referred to as Miller's instability (Miller 1964). Recently Helmi & Gomez (2007), hereafter HG, showed this is a generic feature of Hamiltonian dynamics and not, as long believed, an artifact specific to N-body integrations (Hemsendorf & Merritt 2002; Kandrup & Sideris 2003). HG discuss the effect in detail for spherical potentials. All our tests with spherical, axisymmetric and triaxial potentials show a similar quasi-exponential initial decay. Since DaMaFlow integrates the equations of motion for a single particle in a perfectly smooth potential, it is evident that this behaviour has nothing to do with N-body effects.

A NAFF frequency analysis of particle orbits in the Eddington potential reveals, as expected, three linearly independent frequencies. It is this number that dictates the speed with which stream densities decrease in static, separable potentials. One can see this

---

[6] Orbits starting on axes of symmetry in phase-space can show non-generic stream density behaviour for $\underline{\underline{V}}_x(\overline{x}_0) = \underline{0}$ as we will discuss in the section on non-integrable potentials (section 5).

[7] These values do not have any specific meaning. We have chosen them just in a convenient way.
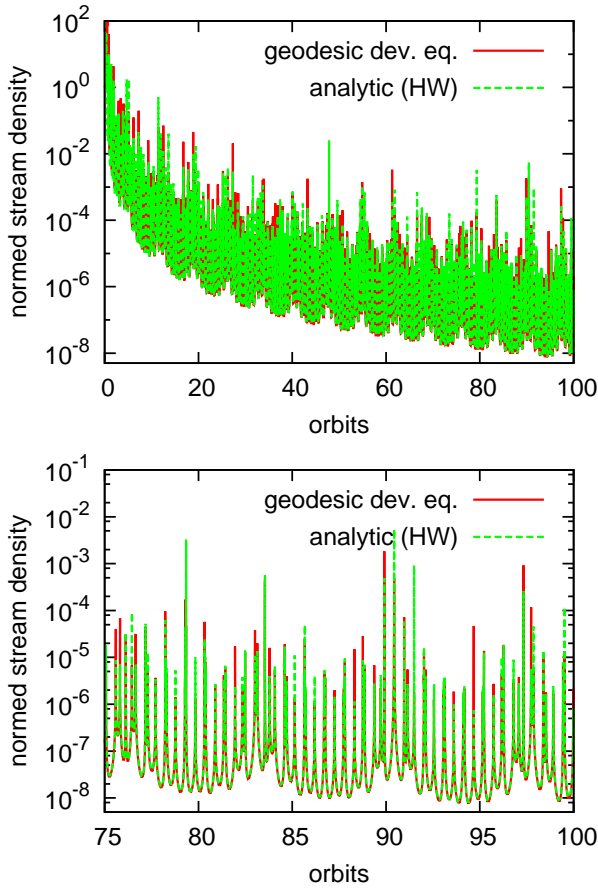
Figure 5. Stream density evolution for the normal Kepler potential ($\alpha = 1$) and for a modified potential ($\alpha = 0.75$). Orbits in the Kepler potential have a single fundamental frequency. Changing the potential exponent from $\alpha = 1$ to $\alpha = 0.75$ increases the number of fundamental frequencies to two. As a result, the long-term stream density behaviour changes from $1/(t/t_{\mathrm{orbital}})$ to $1/(t/t_{\mathrm{orbital}})^2$. For integrable potentials the long-term stream density decrease on each orbit is dictated by the number of fundamental frequencies.

Figure 4. The stream density evolution calculated using the GDE integrator DaMaFlow is compared to the analytic result obtained by a linearised treatment in action/angle variables (Helmi & White 1999). The results agree essentially perfectly. Notice how well the numerical calculation matches the caustics. The upper panel clearly shows that the numerical result also has the correct $1/(t/t_{\mathrm{orbital}})^3$ behaviour at late times. The initial quasi-exponential decay is also visible.

very clearly from Fig. 5. Here we show the density decrease in a simple Kepler-like toy-model:

$$\Phi(r) = -\frac{1}{r^\alpha}. \qquad (32)$$

For $\alpha = 1$ the orbit was started from $\underline{x}_0 = (-0.33, 0.97, 0)$ and $\underline{v}_0 = (-1.0, -0.07, 0)$ with an energy $E = -0.5$. This orbit has only one fundamental frequency. Changing α to 0.75 increases the number of frequencies to two; the loops of the orbit no longer close. The starting point for this second case has been set to $\underline{x}_0 = (-0.27, 1.28, 0)$ and $\underline{v}_0 = (-0.76, 0.24, 0)$, corresponding also to $E = -0.5$. The increased number of frequencies results in a more rapid decrease in stream density: $1/(t/t_{\mathrm{orbital}})$ for one fundamental frequency, and $1/(t/t_{\mathrm{orbital}})^2$ for two. In this sense the long-term behaviour of streams in static, integrable systems is very simple and is determined only by the number of fundamental frequencies.

5 NON-INTEGRABLE POTENTIALS

Analytic methods like the HW formalism are only able to deal with integrable potentials. This is a serious limitation since realistic po-
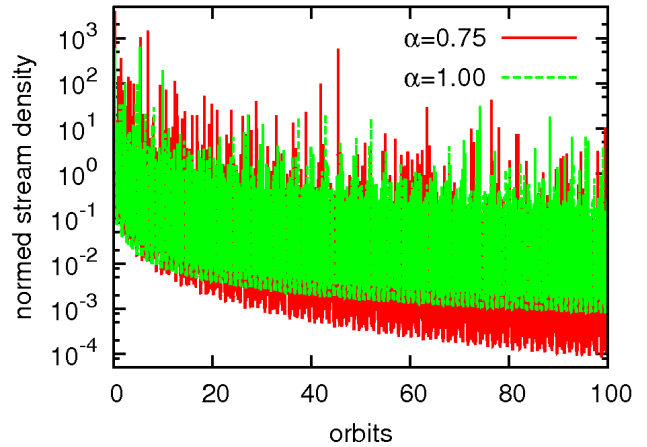
tentials are rarely integrable. To demonstrate that the GDE method can also deal with more complex phase-space structure we now discuss the well-known ellipsoidal logarithmic potential with a core,

$$\Phi(x, y, z) = \frac{1}{2}v_0^2 \ln\left(r_c^2 + x^2 + (y/q)^2 + (z/p)^2\right), \qquad (33)$$

analysing its stream density behaviour and its phase-space structure. There are two reasons why we have chosen this potential: first there has been substantial previous work on its phase-space structure (Binney & Spergel 1982; Papaphilippou & Laskar 1998), so we can compare directly with these earlier results. Second this potential is often considered as a good model for galactic halos because it reproduces a flat rotation curve and its shape can easily be tuned by two parameters that correspond to the axial ratios of the ellipsoidal isopotential surfaces. It has been used, for example, for dynamical studies of the debris streams of the Sagittarius dwarf galaxy (Helmi 2004). The ellipsoidal logarithmic potential without a core ($r_c = 0$) has also been used to study the influence of halo shape on the annual modulation signal in dark matter detectors (Evans et al. 2000).

It is known that, depending on the degree of triaxiality, the phase-space of the logarithmic potential can be occupied to a large extent by chaotic orbits (Papaphilippou & Laskar 1998). In Fig. 6 we show how the stream density evolves along one of these chaotic orbits. This orbit was integrated in a potential with $q = 1.5, p = 0.5, v_0 = 1, r_c = 1, E = 3$ and started at $\underline{x}_0 = (10, 1, 5), \underline{v}_0 = (0.16, 80, -0.16)$. Here we apply the same system of units as Papaphilippou & Laskar (1998) and write all quantities as dimensionless numbers. It is evident from this plot that the system mixes very rapidly along this orbit. This is chaotic mixing, and contrasts with the phase mixing that we found before for regular motion in separable potentials. We note that chaotic orbits are difficult to handle from a numerical point of view because of the rapid spread in phase-space that characterises them. To check whether we can rely on our stream density values, we also calculated the 6-D phase-space density along this orbit. Over the full
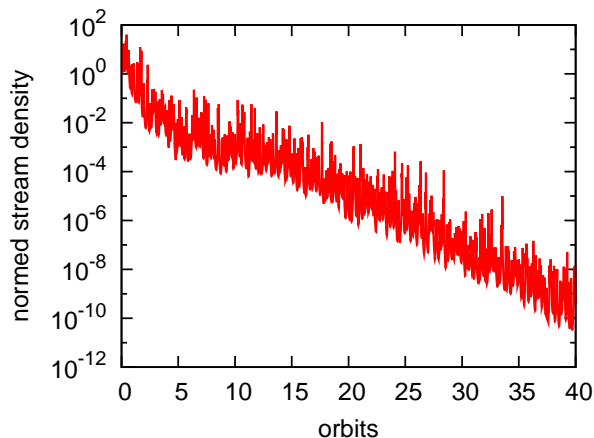
Figure 6. Stream density evolution along a chaotic orbit in the ellipsoidal logarithmic potential with $q = 1.5, p = 0.5$. The density decreases very rapidly, reflecting the chaotic mixing along this orbit. Note that the decrease is no longer a power-law, as in the case of regular motion.

integration range shown in Fig. 6 (40 orbits) it remained constant to an accuracy of 10^{-7}.

Using DaMaFlow we have scanned the phase-space of box orbits within the logarithmic potential, identifying chaotic and regular regions by calculating the stream density evolution for about 5×10^4 different orbits. Each orbit was integrated for a fixed time interval of 2000 using 2×10^5 time-steps. This corresponds to about 10^3 orbital periods. We chose this very long integration time in order to distinguish between chaotic and regular regions[8].

Our results can be compared directly to previous work where the same potential was analysed using frequency shifts (Papaphilippou & Laskar 1998). This method is based on the fact that chaotic motion, contrary to regular motion, has no stable fundamental frequencies, so that frequency estimates shift with time. By looking for such shifts one can distinguish between chaotic and regular motion. Fig. 7 shows maps of orbit type for two different sets of axial ratios q, p. This figure can be compared directly to Fig. 6(c) and Fig. 4(b) in Papaphilippou & Laskar (1998). For the first of these calculations we adopted the following values: $q = 1.8, p = 0.9, v_0 = \sqrt{2}, r_c = 0.1$ and $E = -0.404858$. For the second case we changed the potential shape by instead taking $q = 1.1, p = 0.9$.

The maps of Fig. 7 are constructed as follows. We start each orbit at the centre of the potential to be sure to get a box-orbit with zero angular momentum. Each individual orbit can be labelled by its initial v_x and v_y velocity components. The value of v_z is then determined by the chosen value of the energy, $E = -0.404858$. This is, of course, a very special point within the potential, and it turned out that our standard choice of initial stream orientation, $\underline{V}_x(\overline{x}_0) = \underline{0}$, produces highly non-generic stream density behaviour in this case; the stream density remains constant! In order to get properly representative behaviour we therefore took $\underline{V}_x(\overline{x}_0) = \underline{1}$ when producing Fig. 7. With this set-up, we scanned the whole $v_x - v_y$ plane and saved the stream density of each orbit after a fixed amount of time. The greyscale in the plots corresponds

to the stream density decrease after that fixed time. Black points denote a very rapid stream density decrease, thus regions of chaotic mixing. Grey regions show a slower density decrease, reflecting phase mixing and regular motion. Much of the box-orbit phase-space is chaotic for $q = 1.8, p = 0.9$. Reducing the asphericity to $q = 1.1, p = 0.9$ results in a much larger fraction of the boxes being regular.

A comparison of Fig. 7 to Fig. 6(c) and Fig. 4(b) in Papaphilippou & Laskar (1998) shows excellent and detailed agreement. Regions of high frequency shift correspond, as expected, to those of rapid stream density decrease and chaotic mixing. Thus the GDE and the frequency shift technique work equally well for delineating regions of chaotic and normal phase mixing. We note that the Lyapunov exponent technique for identifying chaotic behaviour is closely related to the GDE (Lichtenberg & Lieberman 1983; El-Zant 2002), since these exponents are obtained from the eigenvalues of the 6D distortion tensor. Identifying and characterising chaotic behaviour is not the main goal of our work here, so we will not pursue this connection further in this paper.

So far we have classified orbits as either regular or chaotic, but the regular part of phase-space has substructure in the form of resonances (Carpintero & Aguilar 1998; Wachlin & Ferraz-Mello 1998; Merritt & Valluri 1999). These are regions where the frequencies of motion are commensurate $m_1\omega_1 + m_2\omega_2 + m_3\omega_3$ where the m_i are integers and the ω_i are the three frequencies of the regular motion. As shown above, resonance influence the stream density behaviour over long timescales (Helmi & White 1999; Siegal-Gaskins & Valluri 2007). This is because they restrict the motion to a lower dimensional region in phase-space, implying that the orbit does not fill its KAM (Kolmogorov-Arnold-Moser) torus densely. In simple terms, the system cannot spread as fast as it would do in the non-resonant case because it occupies a space of lower dimension.

Fig. 8 shows the stream density evolution along three different box orbits for $q = 1.8, p = 0.9, v_0 = \sqrt{2}, r_c = 0.1, E = -0.404858$. The initial conditions for these orbits were chosen so that they have different numbers of orbital resonances (non-resonant, one resonance, two resonances): $\underline{x}_0 = (-0.08, -0.70, -0.090), \underline{v}_0 = (-0.60, -1.50, -0.07)$, $\underline{x}_0 = (-0.01, -0.67, -0.08), \underline{v}_0 = (-0.53, -1.60, -0.06)$ and $\underline{x}_0 = (0.08, -0.63, -0.14), \underline{v}_0 = (-0.51, -1.51, -0.52)$. It is clear that the number of resonances has a major effect on the final stream density decrease over timescales similar to those shown in this plot. The difference in stream density between the non-resonant case and the case with two resonances is about 3 orders of magnitude after 350 orbits! Resonances also have a strong influence on the shape of the orbit in configuration-space, as shown in the lower panel of Fig. 8. Two resonances restrict the orbit to a line. From the shape of the orbits it is evident why the stream density changes so much with the resonances. The particles cannot spread over a large region if they are confined to a space of small dimension.

The regular region of phase-space for the logarithmic potential is occupied by resonant and non-resonant regions. We used DaMaFlow to scan the regular region (as for the chaos maps above) and fitted the stream density decrease by a power law in time. A non-resonant motion then gives an exponent of 3, whereas regions with two resonances should give 1. We binned these power law exponents (bin size 0.1) and coloured them. The result of this procedure is shown in Fig. 9. For this map we integrated a total 450×450 orbits for about 10^4 orbital periods. Each integration required 25×10^6 KDK leapfrog time-steps. The chaotic regions are

---

[8] For chaotic orbits elements of the distortion matrices can become very large. Here we are only interested in separating chaotic and regular orbits reliably. Thus we do not care about round-off errors in the calculation of these matrices.
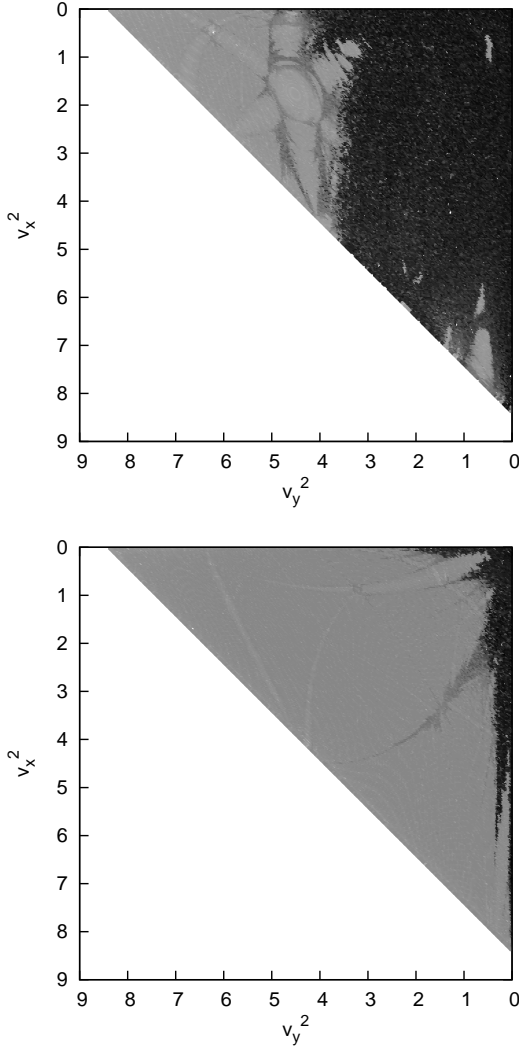
Figure 7. Chaos maps for box orbits in the logarithmic ellipsoidal potential for two different sets of axial ratios. The upper plot is for a highly aspherical potential with $q = 1.8, p = 0.9$, whereas the lower plot is for a rounder potential with $q = 1.1, p = 0.9$. The greyscale indicates the stream density decrease after a fixed time interval (2000 time units or about 100 orbital periods). Black regions mark the very low final stream densities found for chaotic orbits, while grey regions mark the higher stream densities found for regular orbits. Densities decay quasi-exponentially in the former case, but only as a power law of time in the latter. These plots can be directly compared to Fig. 6(c) and Fig. 4(b) in Papaphilippou & Laskar (1998), where a frequency shift analysis of the same system reveals exactly the same structures.

shown in grey, while the regular regions are shown in three different colours depending on their stream density behaviour. We note that the chaos detection here was carried out by imposing a threshold 10^{-15} on the stream density decrease. Every orbit that crosses this threshold during its evolution is considered as chaotic and marked as grey in the map. This is the reason why the chaotic pattern here is not identical to that in Fig. 7.

Most of the regular phase-space in this figure is occupied by non-resonant orbits shown in green. Superposed on these is a fine network of resonance lines shown in red. In blue regions the stream density decreases linearly with time because there are two resonances. Note how well our method locates the res-
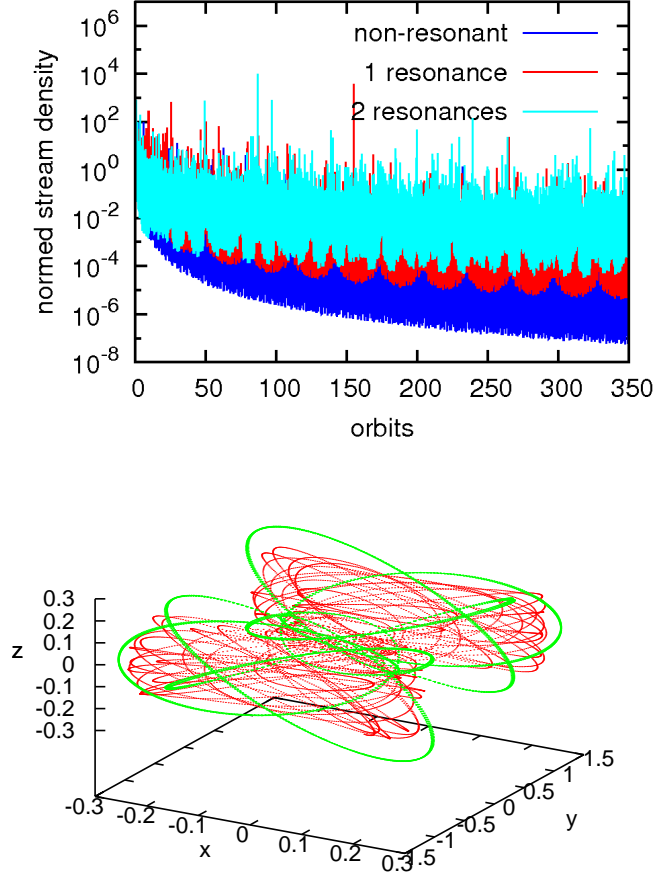
Figure 8. Stream density evolution on resonant orbits. Stream density drops at a rate which depends on the number of independent orbital frequencies. Non-resonant orbits have three independent frequencies, and their stream density decreases like $(t/t_{\mathrm{orbital}})^{-3}$ at late times. Resonances reduce the number of independent frequencies and slow the decrease of stream densities. With one resonance there are two independent frequencies; the stream density then falls as the inverse square of time. With two resonances, only one independent frequency remains and density falls as the inverse first power of time. The number of resonances also strongly affects the orbit shape in configuration-space. As is visible for the examples in the lower plot, non-resonant orbits (red) fill a 3D volume, whereas orbits with two resonances (green) are restricted to a line.

onance lines in the initial condition space spanned by v_y and v_x. Papaphilippou & Laskar (1998) analysed resonances with frequency maps by plotting the rotation numbers defined as $a_1 = \nu_L/\nu_S$ and $a_2 = \nu_M/\nu_S$, where ν_i are the fundamental frequencies along the long (L), short (S) and middle (M) axes. It is straightforward to identify the resonance lines in Fig. 9 with those in the frequency map of Papaphilippou & Laskar (1998) by applying a NAFF frequency analysis to the orbit corresponding to any specific initial condition, for example, one on a given resonance line. It turns out that we can identify all resonance lines in Fig. 9 with similar lines in the frequency map. At the intersection of these lines we have periodic orbits (satisfying two resonance conditions) with the same rotation numbers as those found in Papaphilippou & Laskar (1998). For example, the line going from the upper left corner to the lower right corresponds to the $(3, 1, -2)$ resonance, meaning that $3a_1 + 1a_2 - 2 = 0$.
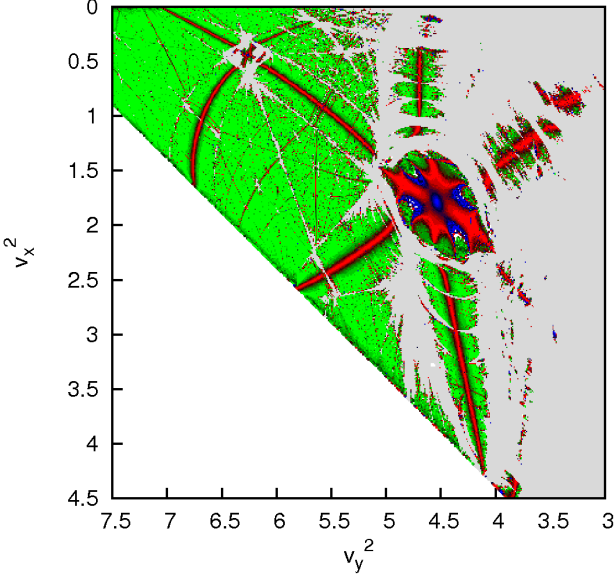
Figure 9. Resonance structure of a logarithmic potential as revealed by the GDE. Green indicates regions with no resonance (i.e. three independent orbital frequencies). Stream densities for these orbits decrease as $(t/t_{\mathrm{orbital}})^{-3}$ at late times. Red indicates orbits with one resonance, for which stream densities decreases as $(t/t_{\mathrm{orbital}})^{-2}$. Orbits with two resonances are coloured blue. This map was constructed by integrating 450×450 orbits, each for about 10^4 orbital periods, using DaMaFlow in parallel. Each orbit required 25×10^6 time-steps using a KDK leapfrog algorithm.

We conclude that our method can resolve the structure of phase-space equally as well as the standard frequency mapping technique.

6   TRIAXIAL DARK MATTER HALOS

In CDM cosmologies dark matter halos are not spherical. Furthermore, simulations suggest that their shape should vary with radius, both equidensity and equipotential surfaces being rounder (on average) at larger radii. Several studies have tried to constrain the shape of the Milky Way's halo by analysing the properties of observed tidal streams like that of the Sagittarius dwarf galaxy (Ibata et al. 2001; Helmi 2004). Recently, Hayashi et al. (2007) analysed the radial variation in potential shape of simulated halos that might correspond to that of the Milky Way. Although there is substantial object-to-object scatter, on average they found a relatively rapid transition from aspherical to almost spherical which occurs near the scale radius r_s of the best fitting NFW profile. They provide a simple fitting formula for this mean behaviour,

$$\log\left(\frac{b}{a} \text{ or } \frac{c}{a}\right) = \alpha\left[\tanh\left(\gamma \log \frac{r}{r_\alpha}\right) - 1\right], \qquad (34)$$

for the principal axial ratios b/a and c/a. (Note that they actually provide two different sets of fitting parameters for Eq. (34) depending on the principal axial ratios.) They also propose a modified NFW potential that takes into account the variation in shape, but this potential is not very convenient because it is not straightforward to derive the corresponding equations of motion. The examples given above show that potential shape can have a substantial
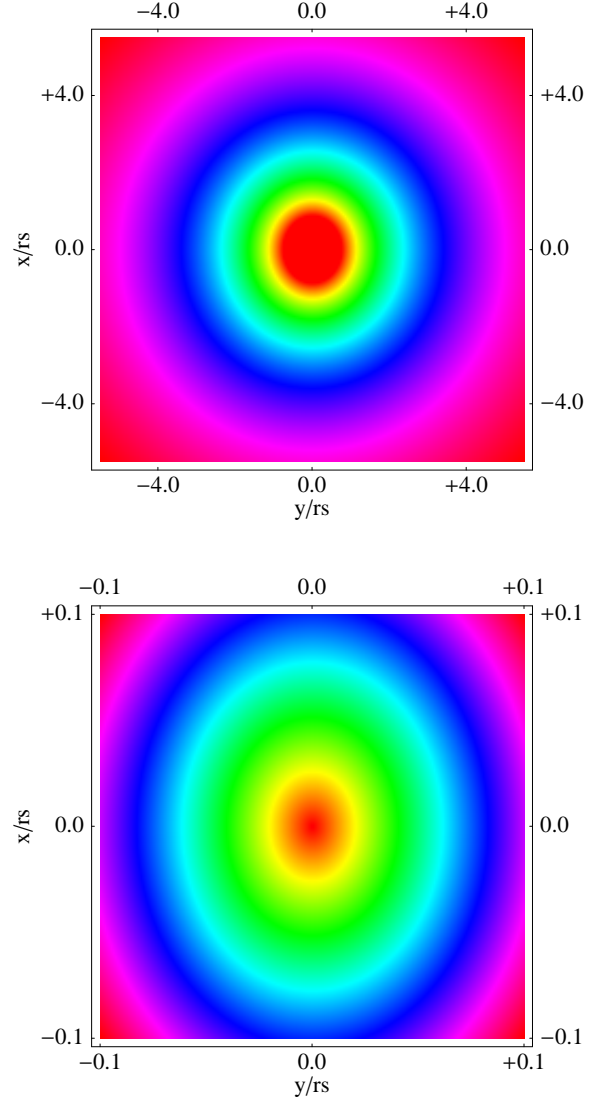

Figure 10. Isopotentials for the outer and inner parts of one of our triaxial NFW halos. It is obvious that the halo becomes rounder as one moves outwards. In this case the transition scale r_a was chosen to be equal to the scale radius r_s of the NFW profile.

effect on stream density evolution, so it is interesting to see how strong such effects can be in a realistic model.

To analyse this we have built a simple extension of the NFW model that qualitatively reproduces the shape variation found by Hayashi et al. (2007) but which has simple equations of motion that can easily be implemented in DaMaFlow. (For another similar model, see Adams et al. (2007).)

We model the variable shape of the NFW halo by replacing the euclidean radius in the formula for the potential of a spherical NFW halo by a more general "radius" $\tilde{r}$ given by:

$$\tilde{r} = \frac{(r_a + r)\, r_E}{(r_a + r_E)}. \qquad (35)$$

Here r_a is a transition scale where the potential shape changes from ellipsoidal to near spherical and r_E is an ellipsoidal "radius" given
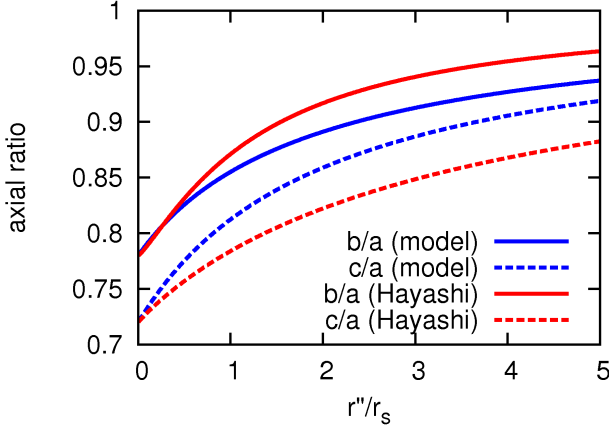
Figure 11. Comparison of the radial variation of isopotential axial ratios for N-body halos (Hayashi et al. 2007) to that for our simple triaxial NFW model. The N-body values are the average of those found in Hayashi et al. (2007). The transition scale r_a of our model has been set equal to the scale radius r_s of the underlying NFW profile.

by:

$$r_E = \sqrt{\left(\frac{x}{a}\right)^2 + \left(\frac{y}{b}\right)^2 + \left(\frac{z}{c}\right)^2}, \qquad (36)$$

where we require $a^2 + b^2 + c^2 = 3$. Thus for $r \ll r_a$ $\tilde{r} \cong r_E$ and for $r \gg r_a$ $\tilde{r} \cong r$. We then take the potential to be $\Phi(x, y, z) = \Phi_{\mathrm{NFW}}(\tilde{r}(x, y, z))$ which reproduces the general behaviour found by Hayashi et al. (2007) with a smooth transition around r_a.

For a specific example, we have chosen the transition scale to be the scale radius of the NFW profile and have taken values for a, b and c that give central principal axial ratios that are comparable to those found by Hayashi et al: $b/a = 0.78$ and $c/a = 0.72$. Our choice is $a = 1.18, b = 0.92, c = 0.85$. For the NFW profile we used a concentration of $r_{200}/r_s = 7.0$. We checked Poisson's equation for this potential to ensure that it implies a positive density everywhere. The check was performed by DaMaFlow evaluating the negative of the trace of the tidal field on a fine 3D grid. This is just the Laplacian of the potential and so proportional to the corresponding density. Since the density field is continuous, positive density values on the grid should guarantee a positive density everywhere.

Fig. 10 shows isopotentials in the outer and inner parts of the halo. All distances are expressed in terms of the scale radius r_s of the NFW profile. The transition from spherical to aspherical can clearly be seen as the centre is approached. Fig. 11 compares the radial variation in axial ratios in our model and in the simulations of Hayashi et al. (2007). The simulation axial ratios are calculated with eq. (34) using the average values for α, γ, r_α found in Hayashi et al. (2007). The lines for our model are calculated as follows. For a given value of $\tilde{r}$ we computed the intersections of the corresponding isocontour with the x, y and z axes. So we get three values a'', b'', c''. To look for their variation over distance we define the mean distance $r'' = \sqrt{(a'')^2 + (b'')^2 + (c'')^2}$. This is essentially the same procedure which Hayashi et al. (2007) applied when fitting the isopotentials of their simulated halos. Thus we can compare directly with their results as in Fig. 11. The qualitative behaviour of our model is very similar to that of the simulations. It is not necessary to demand an exact fit since the scatter between different halos studied by Hayashi et al. (2007) is quite large.

We implemented this potential into DaMaFlow and looked at

four different orbits with the following apo-/pericentre distances in units of r_s: 8.9/6.1, 20/5.9, 2.2/0.5, 1.2/0.4. We compared the stream densities predicted for our triaxial model to those predicted in the corresponding spherical NFW profile. We fixed the starting point and the velocity direction to be the same in the two cases. The amplitude of the velocity was then set to give the same energy in the two cases. With this procedure the orbits covered comparable regions in configuration-space and had nearly the same apo- and pericentre distances. Note that it is impossible to get identical orbital shapes in the two potentials. Especially in the inner parts of the halo, where the two potentials differ substantially, the orbits have different shapes. In a spherical potential orbits are confined to a plane by conservation of angular momentum, but this is not the case in a triaxial potential.

In Fig. 12 we show the stream density evolution for these four orbits. Two belong to the outer halo with peri- and apocentre beyond the scale radius. As expected their stream density behaviour is very similar in the two potentials. As soon as orbits penetrate the inner halo, however, the behaviour is quite different in the two cases. After 100 orbits, streams are about 100 times less dense in a triaxial halo than in a spherical one. Note that this is just what one would predict, given the $(t/t_{\mathrm{orbital}})^{-2}$ and $(t/t_{\mathrm{orbital}})^{-3}$ density evolution expected for regular motion in spherical and triaxial potentials, respectively.

In the case of a cored ellipsoidal potential we showed above that, depending on the level of triaxiality, substantial fractions of phase-space can be occupied by chaotic orbits. Thus we may expect such orbits to be present in our triaxial NFW profile also. Previous work on galactic dynamics has demonstrated the presence of chaotic orbits in the potentials corresponding to a variety of cuspy, triaxial density profiles (Merritt & Fridman 1996; Merritt & Valluri 1996; Valluri & Merritt 1998; Kandrup & Siopis 2003; Capuzzo-Dolcetta et al. 2007). To search for chaotic orbits in our model, we have integrated 2×10^4 different representative orbits and studied the predicted behaviour for the density of their associated streams. For simplicity we have chosen the initial conditions for these orbits at random from the known analytic distribution function of a Hernquist sphere matched to the mean radial density profile of our triaxial NFW model. A self-consistent Hernquist sphere has density profile and potential:

$$\rho(r) = \frac{M}{2\pi} \frac{a}{r} \frac{1}{(r + a)^3}; \quad \Phi(r) = -\frac{G M}{r + a}. \qquad (37)$$

We match to our NFW model by an appropriate choice of the scale length a (Springel et al. 2005). A standard inversion technique can then be used to select a random set of initial orbital positions from this (spherically symmetric) distribution. Appropriate initial velocities can be generated by applying the von Neumann rejection technique (Press et al. 1992; Ascasibar & Binney 2005) to the analytically known distribution function of the self-consistent Hernquist model (Hernquist 1990). This procedure does not, of course, sample orbits with a weighting which would self-consistently reproduce our triaxial NFW model. Nevertheless, the similarity of the NFW and Hernquist models should ensure that our selected orbits cover the regions of phase-space which would be populated in a truly self-consistent model in a reasonably representative way. This is sufficient to evaluate the overall importance of chaotic orbits in the model.

We integrated each orbit as long as required to guarantee $\max(x_{\mathrm{cross}}, y_{\mathrm{cross}}, z_{\mathrm{cross}}) = 10^3$, where i_{cross} is the number of crossings along the i-coordinate, $i = x, y, z$. The integration was done by the Dop853 algorithm with a very high precision to get an
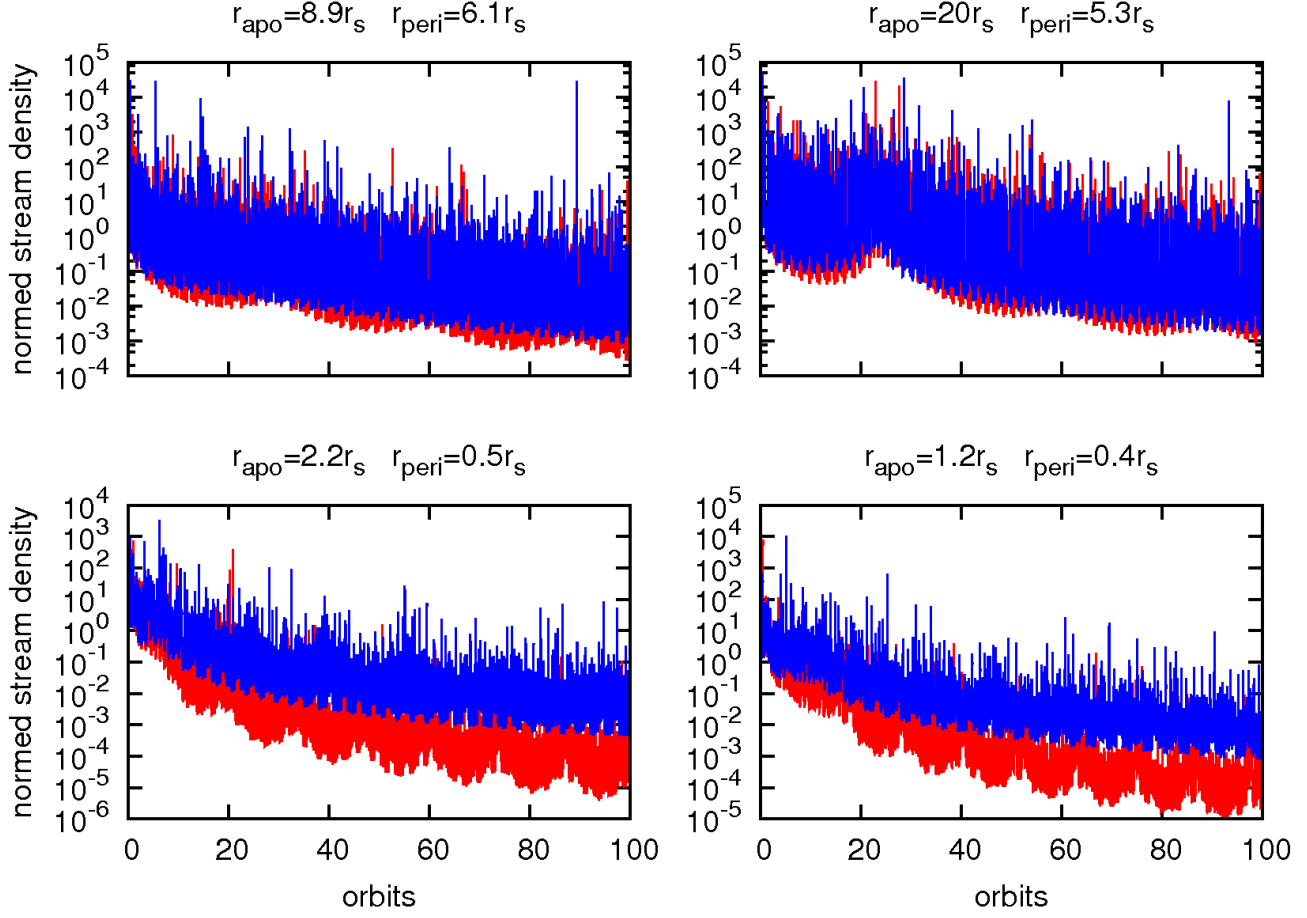
Figure 12. Stream densities in a spherically symmetric NFW potential are compared to those expected in a more realistic DM halo with a shape that varies with radius. Orbits with pericentre inside the transition scale $r_a = r_s$ show a substantial difference between the two cases. After about 100 orbits streams are roughly 100 times less dense in a triaxial halo than in a spherical one. Thus spherical models for the Milky Way's halo are likely to underestimate the number of streams in the solar neighbourhood by two orders of magnitude.

relative energy error below 10^{-10} over the whole integration time. We have chosen such high energy conservation to be sure that the integration works correctly even though the potential is cuspy.

We plot the final stream stream density using a greyscale just as in Fig. 7. The axes of the resulting plots in Fig. 13 are the orbital energy in the triaxial NFW potential and the circularity based on the spherical Hernquist profile that was used to generate the initial conditions. Black points correspond to very large decreases in stream density, hence to non-regular motion. The upper panel shows all orbits whereas the lower panel takes only box orbits into account. We distinguished box and tube orbits by looking at the angular momenta around the symmetry axes. For a box orbit the sign of all three momenta changes along the orbit. On the other hand a tube orbit has one axis along which the angular momentum has a fixed sign.

First of all it is quite striking from these plots that there are orbits that are not regular and show up as black points. A line of fixed pericentre ($1/3r_s$) in Fig. 7 clearly shows that these are orbits that reach the innermost part of the halo, where they feel the strong triaxiality and the cusp. This is not surprising because previous studies showed that cuspy, triaxial potentials exhibit chaos

(Valluri & Merritt 1998; Kandrup & Siopis 2003). These studies found that box orbits are primarily affected but also some tube orbits. This behaviour can clearly be seen in Fig. 13

It is not clear how to distinguish between regular and chaotic motion based on the stream density decrease after a given number of orbital periods. There is no "gap" in the stream density distribution which might separate regular and chaotic motion. Methods like the frequency shift derived from a NAFF analysis run into the same problem (Valluri & Merritt 1998). Lyapunov methods are better suited to this problem, but may also have problems making a clear distinction (Kandrup & Sideris 2002). As our objective here is not a precise chaos analysis of our triaxial NFW potential, we take a fiducial value of 10^{-25} for the stream density which separates regular and chaotic motion. This value is based on the stream density distribution function and corresponds to a stream density below the "regular motion bump". Orbits with a stream density below 10^{-25} will be considered as chaotic. With this criterion about 35% of the orbits with binding energy between $0.91 |E_0|$ and $1.00 |E_0|$ are chaotic. This fraction is not particular high compared to previous studies. Valluri & Merritt (1998), for example, find fractions up to 80% depending on the parameters they use for their triaxial density
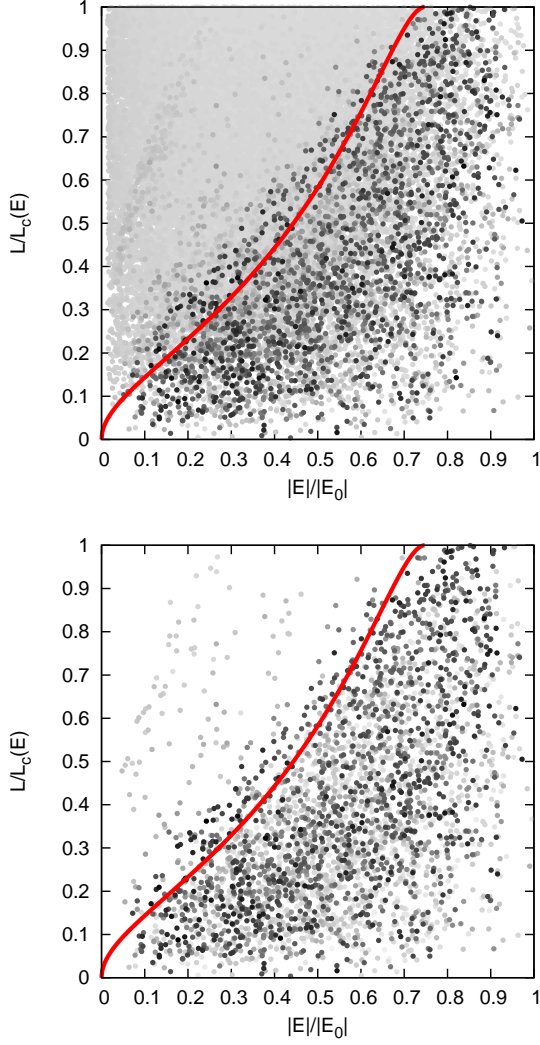
Figure 13. Qualitative view of the phase-space structure of our triaxial NFW potential. These plots give results for 2×10^4 orbits. The greyscale represents the stream density decrease after $\max(x_{\mathrm{cross}}, y_{\mathrm{cross}}, z_{\mathrm{cross}}) = 10^3$. Black points correspond to orbits with a very strong density decrease, thus to non-regular orbits. Such orbits are found primarily in the inner regions of the potential. Orbits with lower binding energy are mostly regular, showing a much smaller stream density decrease. The black points were plotted last to avoid over-plotting by the grey ones. E_0 corresponds to a particle at rest at the centre of the potential. The solid red line represents the constant pericentre line ($r_{\mathrm{peri}} = 1/3 r_s$). In the lower panel only the box orbits are plotted. Most of the non-regular orbits are boxes deep inside the potential.

profile. Recent studies of self-consistent models of cuspy triaxial galaxies with dark matter halos (Capuzzo-Dolcetta et al. 2007) also find chaotic orbits to play an important role. Although we have carried out only a qualitative analysis it is clear that chaos plays a role in the centre of our model also. Box orbits are mostly affected by chaotic mixing because they reach the innermost part of the halo. We note that the four orbits shown in Fig. 12 are regular. None of them has a pericentre distance below the "critical" distance $1/3 r_s$.

These results show that stream densities near the Sun are predicted to be much lower for a realistic triaxial potential than for the corresponding spherical potential. The orbital period near the Sun is about 2.5×10^8 yrs and the distance of the Sun from the Galac-

tic Centre is roughly 0.2 to $0.3 r_s$. Figure 12 suggests that mixing will have reduced stream densities from their values at infall by roughly 4 orders of magnitude for typical streams in the solar neighbourhood. Since the mean DM density near the Sun is substantially greater than typical stream densities at infall, we expect at least 10^5 CDM streams to contribute to the density in the solar neighbourhood. We note that this is still likely to be a substantial underestimate, as it is based on a static, smooth halo model and so neglects additional mixing effects which may be important, in particular mixing in precursor objects, mixing due to scattering by halo substructure, and chaotic mixing. Such effects can only be treated properly by applying the GDE to structure formation in its proper cosmological context. This requires the use of N-body simulations. We note that particles orbiting the innermost part of the halo are also affected by the disk potential leading to a non-spherical contribution to the potential.

7   FINE-GRAINED PHASE-SPACE ANALYSIS IN N-BODY CODES

The main motivation of our work is the desire to address issues of mixing and fine-scale structure in full generality by building the GDE into current state-of-the-art N-body codes. We have done this for the current version of the GADGET code (Springel 2005). This is a massively parallel N-body code which has already been used to carry out very large cosmological simulations (Springel et al. 2005). It calculates the gravitational forces with an efficient TreePM method (Bode et al. 2000; Xu 1995; Bagla 2002) and uses a domain decomposition scheme based on space-filling (fractal) Peano-Hilbert curves to achieve good work-load balance in parallel operation.

To implement the GDE within GADGET we needed to extend various parts of the code. The dynamics of the distortion tensor are driven by the ordinary gravitational tidal field. The corresponding tidal tensors for each DM particle have to be calculated using the same Tree- or TreePM-Method as the forces in order to provide the correct driving term in the GDE. While the forces are given by the first derivative of the potential, the tidal tensor is made up of second derivatives. The particles in an N-body simulation can be thought of as a Monte-Carlo sampling of the real DM phase-space distribution, but the coarseness of this sampling introduces unwanted discreteness or "two-body" effects which are likely to be more serious for higher derivatives of the potential. Such effects are usually mitigated by softening the gravitational potential of each particle. GADGET uses a spline softening kernel function with compact support:

$$W_2(u) = \begin{cases} \frac{16}{3}u^2 - \frac{48}{5}u^4 + \frac{32}{5}u^5 - \frac{14}{5}, & 0 \leqslant u < \frac{1}{2}, \\ \frac{1}{15u} + \frac{32}{3}u^2 - 16u^3 + \frac{48}{5}u^4 \\ \qquad - \frac{32}{15}u^5 - \frac{16}{5}, & \frac{1}{2} \leqslant u < 1, \\ -\frac{1}{u}, & u \geqslant 1. \end{cases}$$

The softened potential of a point mass is then given by $\Phi^s(\underline{x}) = (Gm/h)W_2(|\underline{x}|/h)$ with a softening length $h = 2.8\epsilon$, where ϵ is the Plummer equivalent softening length. The potential (and so force and tidal field) become Newtonian if $|\underline{x}| \geqslant h$. From this softened potential we can calculate the softened tidal field of a point mass:

$$T_{ij}^s(\underline{x}) = -\frac{\partial^2 \Phi^s(\underline{x})}{\partial x_i \partial x_j} = \delta_{ij} m g_1\left(\frac{|\underline{x}|}{h}\right) + x_i x_j m g_2\left(\frac{|\underline{x}|}{h}\right),$$

where

$$
g_1(u) = \frac{1}{h^3}
\begin{cases}
-\frac{32}{3} + \frac{192}{5}u^2 - 32u^3, & u \leqslant \frac{1}{2}, \\[6pt]
\frac{1}{15u^3} - \frac{64}{3} + 48u \\
\quad - \frac{192}{5}u^2 + \frac{32}{3}u^3, & \frac{1}{2} < u < 1, \\[6pt]
-\frac{1}{u^3}, & u > 1,
\end{cases}
$$

and

$$
g_2(u) = \frac{1}{h^5}
\begin{cases}
\frac{384}{5} - 96u, & u \leqslant \frac{1}{2}, \\[6pt]
-\frac{384}{5} - \frac{1}{5u^5} + \frac{48}{u} + 32u, & \frac{1}{2} < u < 1, \\[6pt]
\frac{3}{u^5}, & u > 1.
\end{cases}
$$

Thus the softened tidal field acting on particle k at position $\underline{x}_k$ (its tidal tensor) is given by:

$$
\begin{aligned}
T_{ij}(\underline{x}_k) =& \sum_{l \neq k} \left[\delta_{ij} m_l g_1 \left(\frac{|\underline{x}_l - \underline{x}_k|}{h} \right) \right. \\
& \left. + (x_{l,i} - x_{k,i})(x_{l,j} - x_{k,j}) m_l g_2 \left(\frac{|\underline{x}_l - \underline{x}_k|}{h} \right) \right] \\
=& \sum_{l} \left[\delta_{ij} m_l g_1 \left(\frac{|\underline{x}_l - \underline{x}_k|}{h} \right) \right. \\
& \left. + (x_{l,i} - x_{k,i})(x_{l,j} - x_{k,j}) m_l g_2 \left(\frac{|\underline{x}_l - \underline{x}_k|}{h} \right) \right] \\
& - \delta_{ij} m_k g_1(0)
\end{aligned}
\tag{38}
$$

The last step highlights a difference between the tidal field calculation and the normal force calculation. The tidal field is obtained using the same tree-walk as the forces. The latter are calculated by evaluating the full sum $\sum_l$ without excluding particle k. This is simply to avoid additional bookkeeping; the particle-particle force vanishes when $l = k$ so including the self-term does not affect the result. This is not the case for the tidal field, for which one must add an extra term to the diagonal tidal tensor elements to remove the self-tidal field. This is similar to the self-energy correction that is needed when using the tree to evaluate the total potential energy of the system.

For larger simulations it is not efficient to use the tree alone. In such cases the TreePM method can be much faster. In this scheme the potential is split into short-range and long-range parts $\Phi = \Phi^{\text{short}} + \Phi^{\text{long}}$. Specifically, in Fourier space GADGET takes

$$
\Phi_k^{\text{long}} = \Phi_k \exp\left(-k^2 r_s^2 \right)
\tag{39}
$$

where r_s defines the spatial scale of the force split and should not be confused with the scale radius of the NFW profile. The long-range potential is calculated by mesh-based Fourier techniques. In Fourier space the tidal field can be calculated by just pulling down $-(ik_j)^2$ with $j = x, y, z$. The short-range potential in real space is given by:

$$
\Phi_{\text{short}}(\underline{x}) = \sum_l \Phi^s(r_l) \operatorname{erfc}\left(\frac{r_l}{2r_s} \right),
\tag{40}
$$

and the corresponding short-range part of the tidal field by:

$$
\begin{aligned}
T_{ij}(\underline{x}) =& \sum_l \left(T_{ij}^s(\underline{x}_l) \left(\operatorname{erfc}\left(\frac{r_l}{2r_s} \right) + \frac{r_l}{\sqrt{\pi} r_s} \exp\left(-\frac{r_l^2}{4r_s^2} \right) \right) \right. \\
& \left. - F_i^s(\underline{x}_l) \frac{x_{l,j} r_l}{2\sqrt{\pi} r_s^3} \exp\left(-\frac{r_l^2}{4r_s^2} \right) \right),
\end{aligned}
$$

where $\underline{F}^s$ is the softened point mass force, $x_{l,i}$ is defined as the smallest distance of any of the periodic images of particle l to the coordinate x_i of $\underline{x}$, and $r_l = \sqrt{x_{l,x}^2 + x_{l,y}^2 + x_{l,z}^2}$.

The time integration also needs modification in order to integrate the GDE in parallel with the equations of motion. For this it is desirable to write both the equations of motion and the GDE in a time-symmetric way. This fits best into GADGET's quasi-symplectic integration scheme which is a second-order leapfrog. For the GDE we need to integrate two differential equations of second-order to solve for $\underline{\underline{D}}_i$ with $i = xx, xv$. Let $\underline{\underline{W}}_i$ denote the first time derivative of $\underline{\underline{D}}_i$. We can then define the system state vector $\tilde{S}$ as,

$$
\tilde{S} = \left(\underline{x}, \underline{v}, \underline{\underline{D}}_{xx}, \underline{\underline{D}}_{xv}, \underline{\underline{W}}_{xx}, \underline{\underline{W}}_{xv} \right)^\dagger.
\tag{41}
$$

The equations of motion and the GDE can now be written as one equation for $\tilde{S}$:

$$
\ddot{\tilde{S}}(t; \overline{x}_0) = f\left(\tilde{S}(t; \overline{x}_0) \right).
\tag{42}
$$

The right hand side does not depend on the time derivative of $\tilde{S}$. This allows the use of a time-symmetric leapfrog scheme with the following Drift- and Kick-operators:

$$
D_t(\Delta t) =
\begin{cases}
\underline{v} & \to & \underline{v} \\
\underline{x} & \to & \underline{x} + \underline{v}\Delta t \\
\underline{\underline{W}}_i & \to & \underline{\underline{W}}_i & i = xx, xv \\
\underline{\underline{D}}_i & \to & \underline{\underline{D}}_i + \underline{\underline{W}}_i \Delta t & i = xx, xv
\end{cases}
\tag{43}
$$

$$
K_t(\Delta t) =
\begin{cases}
\underline{x} & \to & \underline{x} \\
\underline{v} & \to & \underline{v} + \underline{F}\Delta t \\
\underline{\underline{D}}_i & \to & \underline{\underline{D}}_i & i = xx, xv \\
\underline{\underline{W}}_i & \to & \underline{\underline{W}}_i + \underline{\underline{T}}\Delta t & i = xx, xv
\end{cases},
\tag{44}
$$

where $\underline{\underline{T}}$ is the ordinary tidal tensor and $\underline{F}$ the gravitational force. Although the time integration now needs to solve 18 additional non-trivial coupled second-order differential equations, it turns out that the loss in performance is not dramatic, even if we do the calculation for all DM particles in the simulation box. From a computational point of view, the strongest impact comes from the extra memory that is needed to keep track of the distortion tensor. Every particle needs the tidal tensor (6 numbers due to symmetry) and the distortion tensor (36 numbers). Nevertheless, with current computer capabilities this is not a major limitation.

In general the state of an N-body simulation is not stored frequently enough to catch the caustics that occur along each particle's orbit. To avoid missing these we implemented a caustic finder that examines every drift operation of the time integration. As described above, sign changes in the determinant of the configuration-space distortion tensor $\underline{\underline{D}}$ indicate that a particle has passed though a caustic. Whenever this happens the event is logged. We are then limited only by the time-step of the simulation and this is normally small enough to catch all large-scale caustics.

For flexibility in testing, we have also implemented the GDE formalism in a version of GADGET which allows certain static potentials, in particular, NFW, Hernquist and cored ellipsoidal logarithmic potentials, to be included in addition to the self-gravity of the particles.

As a first test of our implementation in GADGET, we have compared the behaviour predicted for N-body realisations of a static Hernquist sphere to that found for an integration in the corresponding smooth potential. To get a system which resembles the Milky Way's halo we take $M = 1.86 \times 10^{12} M_\odot$ and $a = 34.5$
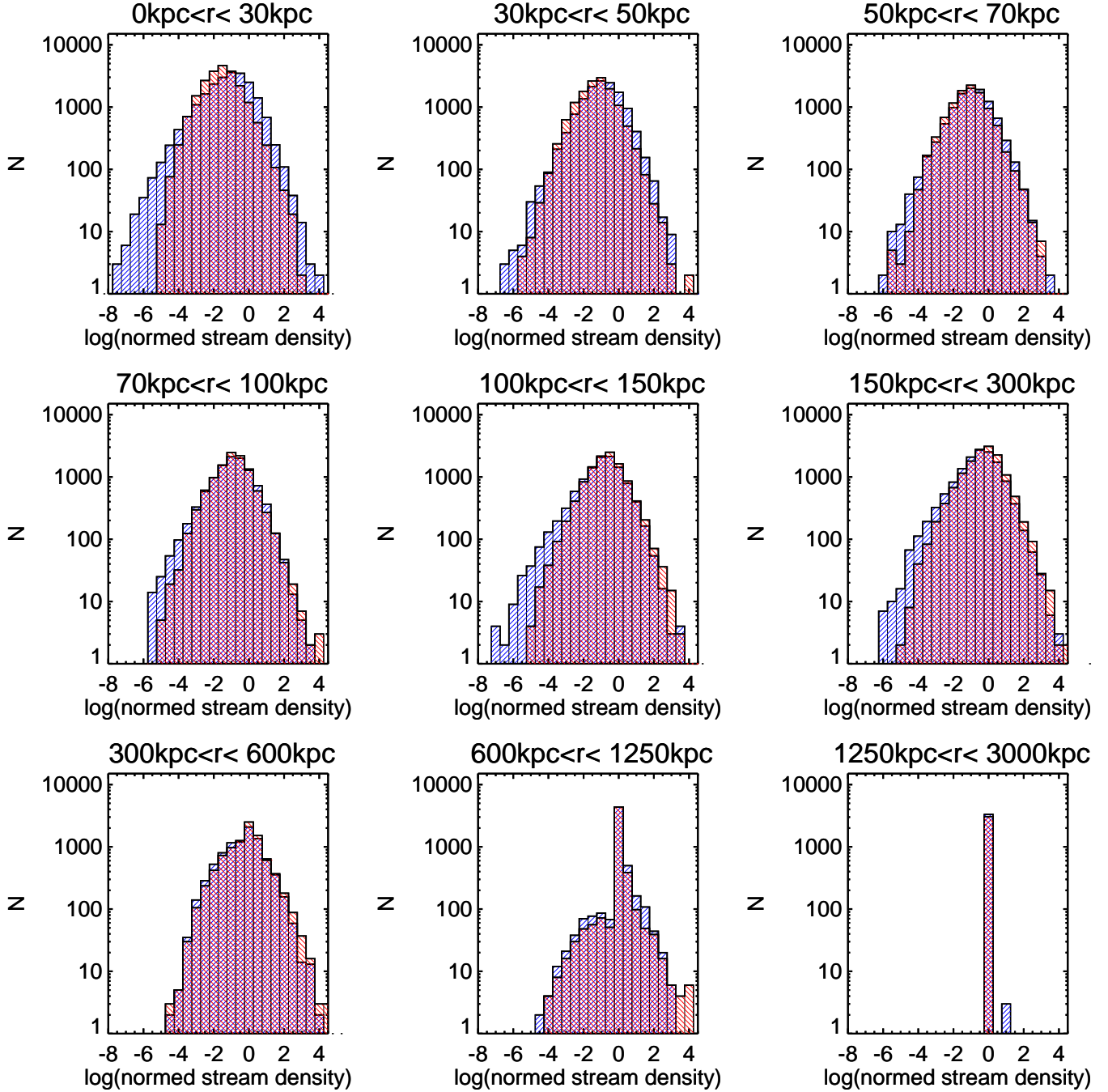
Figure 15. Stream densities for an $N = 10^5$ spherical Hernquist N-body model of the Galactic halo after 5.0 Gyr of integration (blue hatching from bottom left to top right) are compared to those found by integrating from the same initial conditions in the corresponding smooth potential (red hatching from bottom right to top left). In each case the sphere was divided into nine spherical shells and the normed stream densities of all particles in each shell at the final time were histogrammed with bin width 0.5 in log(density). As expected, the lowest stream densities are reached near the centre of the sphere where the dynamical time scale is shortest. In the two outermost spherical shells most of the particles have not yet undergone many caustics. The stream density distribution there has a strong bias towards values > 1. The agreement between the N-body live halo and the smooth potential is good.

kpc in equation (37). The N-body realisation was constructed as described in section 6.

In Fig. 14 we compare the evolution of stream density for a specific orbit in an $N = 10^5$ live Hernquist halo to that found when integrating the same orbit in the corresponding smooth potential. The Hernquist sphere had the parameters given above and the particular orbit chosen here had peri- and apocentre of 25 kpc and 33 kpc, respectively, giving a period of about 0.5 Gyr. It was

integrated for about 15 orbits or 7.5 Gyr. The N-body softening was taken to be $\epsilon = 1.5$ kpc. The 6-D phase-space density remained constant to better than 1 part in 10^8 in both integrations, but the stream density evolution still differs significantly between them, in particular in the timing of the caustics and in the detailed behaviour of the lower envelope. This is a consequence of the well known divergence between nearby orbits in N-body systems which is caused by the cumulative effect of many small perturbations due
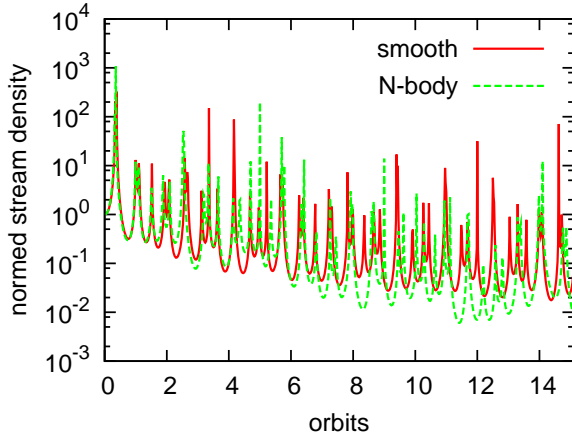
Figure 14. The stream density evolution found by integrating the GDE along an orbit in a live N-body realisation of a Hernquist sphere is compared to that predicted for the same initial condition in the corresponding analytic potential. The N-body halo was realised with $N = 10^5$ particles using a softening length, $\epsilon = 1.5$ kpc. The N-body evolution is very similar in shape and caustic frequency to that in the smooth potential. The 6-D phase-space density remained constant to an accuracy of 10^{-8} over the full N-body integration.

to discreteness (Kandrup & Sideris 2003). The GDE is very sensitive to such noise. The features in the two curves are, nevertheless very similar, in particular the number and spacing of caustics and the overall shape.

Fig. 15 shows the normed stream densities after 5 Gyr of integration for all particles in a live Hernquist halo with $N = 10^5$ and the parameters assumed above. For this integration we adopted $\epsilon = 2.0$ kpc. We divide the particles into 9 radial bins containing approximately equal numbers of particles and then histogram the stream densities, both for the N-body simulation and for integrations from the same initial conditions in a smooth Hernquist potential. Typical stream densities in Fig. 15 decrease towards the centre of the sphere. This is because shorter dynamical times result in enhanced mixing in the inner regions. (Recall that stream densities decrease as $(t/t_{\mathrm{orbital}})^{-2}$ in a spherical potential, and so are smallest where the orbital periods are shortest.) The two outermost radial shells are dominated by particles with long orbital periods which, as a result, have stream densities of order unity. The high stream density tails of the histograms are due to particles which are close to caustic passage. They thus have the universal power-law shape $N(> \rho) \propto \rho^{-1}$ expected near a caustic (see, for example, Mohayaee & Shandarin (2006)).

The two sets of histograms in Fig. 15 are very similar. Although stream densities evolve differently along orbits from a given initial condition in the N-body and smooth potential cases (see Fig. 14) the statistical results for ensembles of initial conditions are similar. N-body discreteness effects do not cause substantial *systematic* shifts in the stream density distributions predicted for this test problem. A small systematic effect is visible at low stream densities. The N-body integration produces more very low-density streams than the integration in the corresponding smooth potential. This is indeed due to discreteness effects, as evidenced by the fact that we find the excess to depend on the N-body softening; smaller softenings result in a larger tail of extremely low-density streams. On the other hand, too large a softening leads to incorrect representation of the mean force near the centre of the system. Thus a trade-off is needed to define the optimal softening. This

has been much discussed with reference to conventional N-body simulations (Merritt 1996; Athanassoula et al. 2000; Dehnen 2001; Rodionov & Sotnikova 2005; Zhan 2006) but we note that the situation is worse for our current application, since the evolution of our extended state vector (equation 42) depends on the tidal tensor. The additional spatial derivative relative to the force makes our GDE integrations substantially more sensitive to discreteness than a standard N-body integration. This suggests that the optimal choice of softening will be larger for GDE integrations than for conventional N-body integrations.

Fig. 15 shows that the high-density tails of the stream density distribution agree well between the N-body and smooth potential integrations. This suggests that the number and the strength of the caustics must be similar in the two cases. We can check this explicitly by again dividing the sphere into radial shells and then calculating the median number of caustic passages by the final time for the particles which end up in each shell. In Fig. 16 we compare the results of this exercise for the N-body and smooth potential integrations using 50 shells. The level of agreement is striking. Only within about 3 kpc of the centre is there a significant difference between the two curves. This is comparable to the softening used for the N-body system, so it is not surprising that particles in this inner core pass through fewer caustics in the N-body case.

The number of caustic passages depends very little N-body parameters. In Fig. 17 we plot median caustic count against radius for two different mass resolutions and for a fixed softening length of 0.5 kpc, four times smaller than in Fig. 16. After 5 Gyr, the highest resolution simulation produces a median caustic count at 1 kpc which agrees with that for the smooth potential integration in Fig. 16, confirming that that the disagreement in that figure was due to the softening of the N-body simulation. It is remarkable that particle number has no strong impact on the median caustic count. The two simulations in Fig. 17 differ by a factor of 32 in particle mass, yet outside 4 kpc they agree very well both with each other and with the more softened integration of Fig. 16. The reason for this stability is that the caustic count is an integer which is augmented only when the determinant of the distortion tensor changes sign. As a result, it is much less sensitive to the exact values of the distortion tensor elements than is the stream density (which depends on the value of the determinant).

We can estimate the median number of caustic passages for particles at radius r very simply as $\kappa t/T(r)$ where t is the age of the system, $T(r)$ the period of a circular orbit at radius r, and κ a proportionality constant. Then $T(r) = 2\pi r/V_c(r)$, where $V_c(r) = \sqrt{GM(r)/r}$ is the circular velocity at radius r. For a Hernquist sphere, the mass $M(r)$ within radius r is $M(r) = Mr^2/(r + a)^2$. Putting all this together we get:

$$c(r, t; \kappa) = \kappa \frac{t}{T(r)} = \frac{\kappa}{2\pi} \frac{t\sqrt{GM/r}}{(r + a)} \tag{45}$$

where $c(r, t; \kappa)$ is the predicted median caustic count at radius r. This estimate works very well, with a best fit $\kappa = 4.2$. The deviation at large radii where the caustic number is low can be accommodated simply by adding a small constant offset, as indicated by the dashed line in the figure. HW (Eq. 37) already showed that caustics occur in a spherical potential when $p_\theta = 0$ or $p_r = 0$, thus at the turning points in the θ and r coordinates. If p_θ and p_r go through zero at different times we would expect four caustics per orbital period. This is surprisingly close to the value of κ that we estimate directly from the simulation, given that the particles seen at radius r actually have a wide range of orbital periods, rather than all having the circular orbit period $T(r)$.
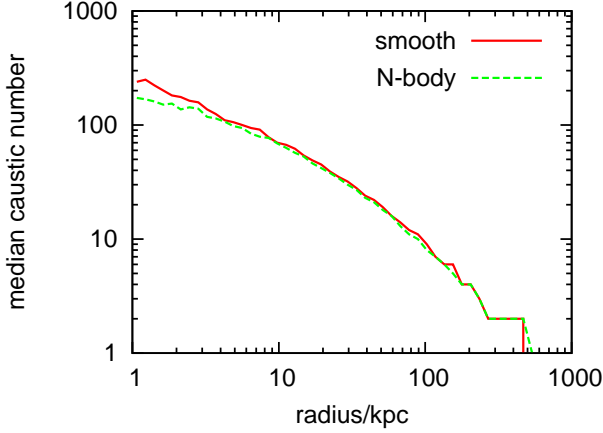
Figure 16. Number of caustic passages after 5 Gyr as a function of final distance from the centre for 10^5 orbits in a Hernquist sphere. The green dashed curve gives the median number of caustic passages at each radius for particles in an N-body realisation of the system integrated with softening parameter, $\epsilon = 2$kpc. The red solid curve shows the result when these same initial conditions are integrated within the corresponding analytic Hernquist potential. The results coincide except within about 1.5 softening lengths of the centre. This demonstrates that caustic counting is very robust against discreteness effects.
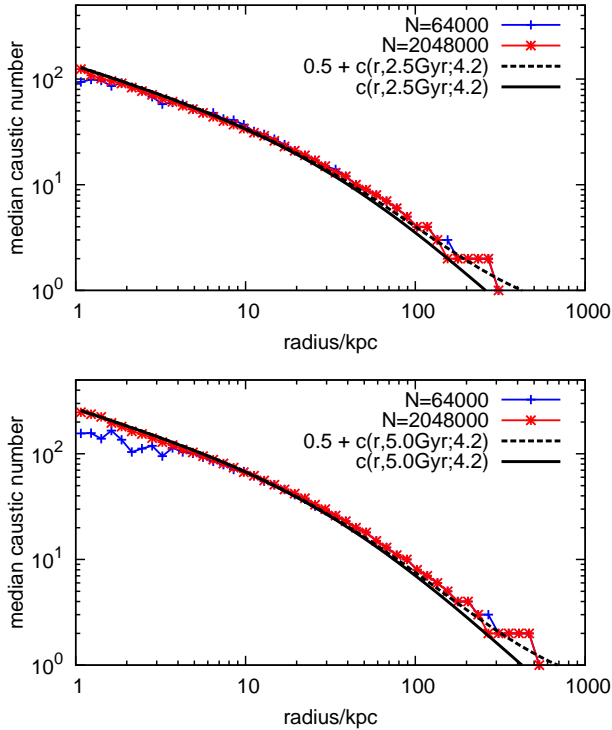

Figure 17. Median caustic passage count against radius, as in Fig. 16, but for different particle numbers and for a smaller softening ($\epsilon = 0.5$ kpc). The panels show results after 2.5 (top) and 5.0 (bottom) Gyr of evolution. Clearly the caustic count goes up between the two times, so the curves are higher in the lower panel. The radial dependence is very well represented by eq. (45). Increasing the number of particles by a factor of 32 has very little effect on these curves, which also agree with those of Fig. 16. This shows that the caustic count along an orbit is very insensitive to the N-body parameters (particle number and softening) used to integrate the system.
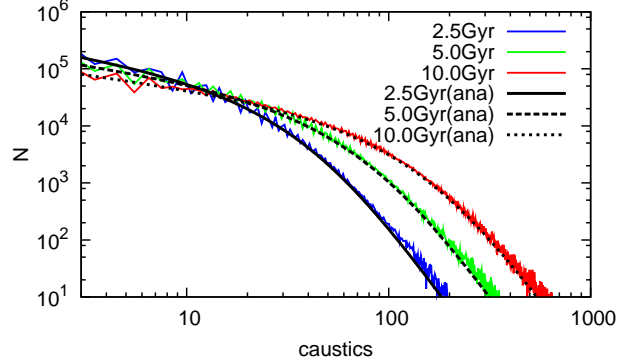

Figure 18. The number of particles that have passed through a given number of caustics is plotted against the number of caustics for our $N = 2048000$ simulation after 2.5, 5 and 10 Gyr. The thin black lines are analytic estimates based on eq. (47).

Rather than focussing on the median count of caustic passages as a function of radius, one can examine the distribution of the number of caustic passages, i.e. the number of particles that have passed through a given number of caustics after some given time. Figure 18 shows such distributions after 2.5, 5 and 10 Gyr for our highest resolution ($N = 2048000$) simulation. With increasing time the characteristic number of caustic passages increases and the number of particles with a small number of caustic passages decreases.

We can make a simple analytic model for these distributions based on Eq. (45). There are $4\pi\rho(r)r^2/m\,\mathrm{d}r$ particles in the interval $(r, r + \mathrm{d}r)$, where m is the mass of a simulation particle and $\rho(r)$ the (analytic) density profile of the Hernquist sphere. If we make the approximation that all particles at radius r have a caustic count equal to the median count predicted by eq. (45), the number of particles with caustic counts in the interval $(c(r, t; \kappa), c(r, t; \kappa) + \mathrm{d}c(r, t; \kappa))$ will be the same as the number of particles in $(r, r + \mathrm{d}r)$, so:

$$f(c)\mathrm{d}c \cong 4\pi\rho(r)\frac{1}{m}r^2\mathrm{d}r \qquad (46)$$

$$= 4\pi\frac{M}{2\pi}a\frac{r(c, t; \kappa)}{(r(c, t; \kappa) + a)^3}\frac{1}{m}\left|\frac{\mathrm{d}r(c, t; \kappa)}{\mathrm{d}c}\right|\mathrm{d}c, \quad (47)$$

where $r(c, t; \kappa)$ is the inverse function of $c(r, t; \kappa)$. As Fig. 18 shows, this formula represents the simulation results very well, suggesting that the variation in caustic count with radius is more important than the scatter in caustic count at given radius for determining the overall shape of the count distribution.

From these first tests we conclude that our N-body implementation is working well, that caustic properties can be predicted very robustly, at least when the caustics reflect large-scale structure in the system, and that stream densities can also be predicted reliably provided care is taken to ensure that discreteness effects are under control.

8 CONCLUSION

Direct DM detection experiments operate on length-scales far below the resolution of current structure-formation simulations. The fine-grained phase-space structure on these scales will determine the signal they see. In addition, small-scale structure can substantially enhance the annihilation signal that is the target of current indirect detection experiments. A better understanding of such struc-

ture within the current concordance ΛCDM cosmology is thus critical for analysing and interpreting all current DM searches.

We propose a new route to tackle these issues. Rather than improving simulations simply by increasing the number of particles, we attach additional information to each particle, namely a phase-space distortion tensor which allows us to follow the evolution of the fine-grained phase-space distribution in the immediate neighbourhood of the particle. We introduce the Geodesic Deviation Equation (GDE) as a general tool for calculating the evolution of this distortion along any particle trajectory. The projection from phase-space to configuration-space yields the density of the particular CDM stream that particle is embedded in and can also identify when the particle passes through a caustic.

This technique makes the fine-grained phase-space structure accessible. It enables studies of the phase-space structure of general non-integrable static potentials which reproduce all the results previously obtained using frequency analysis methods, identifying chaotic regions and finding substructure in regular regions in the form of resonances. In addition, it can be used to quantify mixing rates and to locate caustics. We demonstrate these capabilities for the complex phase-space structure of the ellipsoidal logarithmic potential with a core. All relevant phase-space regions could be identified by solving the GDE along the orbit. We have written a code, DaMaFlow, that allows us to carry out such stream density analyses for a wide variety of potentials in a very efficient way.

Stream density evolution is very sensitive to the shape of the underlying potential. We demonstrate this by comparing results for a realistic CDM halo with radially varying shape to those for a spherical halo with similar radial density profile. After 100 orbits the predicted stream densities in the inner regions differ by a factor of 100. In general we expect the stream densities to decrease as $(t/t_{\rm orbital})^{-3}$ for regular orbits and even faster for chaotic orbits, rather than as $(t/t_{\rm orbital})^{-2}$, the result found for orbits in a spherical potential. Scaling to the Milky Way leads us to estimate that there should be at least 10^5 streams passing through the solar system.

The potentially revolutionary advantage of our approach, and our main reason for pursuing it, is that it applies equally well to non-symmetric, non-static situations of the kind that generically arise in CDM cosmologies. Indeed, it can be implemented in a relatively straightforward way in current state-of-the-art cosmological N-body codes. We have carried out such an implementation in the GADGET code and have presented some tests based on equilibrium Hernquist models. The N-body implementation is able to conserve 6-D phase-space density to high accuracy along individual particle orbits. In addition, it qualitatively reproduces the results found in the corresponding smooth potential for the evolution of stream density along individual orbits, and it reproduces the statistical results found for ensembles of orbits to impressive accuracy. The identification of caustic passages is particularly robust, showing very little dependence on N-body parameters such as particle number and softening. Thus discreteness effects appear to be well under control, at least for the large N systems studied here. The remarkably robust identification of caustic properties makes us optimistic that we will be able to calculate annihilation boost factors due to caustics in fully realistic ΛCDM dark halos.

In future applications we will use these techniques to address mixing and DM detection issues within fully general simulations of the ΛCDM structure formation model.

REFERENCES

Adams F. C., Bloch A. M., Butler S. C., Druce J. M., Ketchum J. A., 2007, arXiv:astro-ph/0708.3101, 708

Akerib D. S., et al 2004, Physical Review Letters, 93, 211301

Aprile E., Baudis L., Cabrera B., 2007, Journal of Physics Conference Series, 60, 58

Ascasibar Y., Binney J., 2005, MNRAS, 356, 872

Athanassoula E., Fady E., Lambert J. C., Bosma A., 2000, MNRAS, 314, 475

Bagla J. S., 2002, Journal of Astrophysics and Astronomy, 23, 185

Bergström L., Edsjö J., Gunnarsson C., 2001, Phys. Rev. D, 63, 083515

Bergström L., Hooper D., 2006, Phys. Rev. D, 73, 063510

Binney J., Spergel D., 1982, ApJ, 252, 308

Blumenthal G. R., Faber S. M., Primack J. R., Rees M. J., 1984, Nat, 311, 517

Bode P., Ostriker J. P., Xu G., 2000, ApJS, 128, 561

Capuzzo-Dolcetta R., Leccese L., Merritt D., Vicari A., 2007, ApJ, 666, 165

Carpintero D. D., Aguilar L. A., 1998, MNRAS, 298, 1

Dalcanton J. J., Hogan C. J., 2001, ApJ, 561, 35

Davis M., Efstathiou G., Frenk C. S., White S. D. M., 1985, ApJ, 292, 371

de Boer W., 2005, New Astronomy Review, 49, 213

de Boer W., Sander C., Zhukov V., Gladyshev A. V., Kazakov D. I., 2005, Physical Review Letters, 95, 209001

Dehnen W., 2001, MNRAS, 324, 273

Diemand J., Kuhlen M., Madau P., 2007, ApJ, 657, 262

Drukier A. K., Freese K., Spergel D. N., 1986, Phys. Rev. D, 33, 3495

Einasto J., Kaasik A., Saar E., 1974, Nat, 250, 309

El-Zant A. A., 2002, MNRAS, 331, 23

Evans N. W., Carollo C. M., de Zeeuw P. T., 2000, MNRAS, 318, 1131

Faber S. M., Gallagher J. S., 1979, ARA&A, 17, 135

Gilmore R., 1982, Catastrophe Theory For Scientists And Engineers. Wiley, Dover, Chichester, Brisbane, Toronto

Hairer E., Norsett S. P., Wanner G., 1993, Solving Ordinary Differential Equations I. Springer Series in Computational Mathematics, Springer Verlag, Berlin

Hayashi E., Navarro J. F., Springel V., 2007, MNRAS, 377, 50

Helmi A., 2004, MNRAS, 351, 643

Helmi A., Gomez F., 2007, arXiv:astro-ph/0710.0514, 710

Helmi A., White S. D., Springel V., 2002, Phys. Rev. D, 66, 063502

Helmi A., White S. D. M., 1999, MNRAS, 307, 495

Hemsendorf M., Merritt D., 2002, ApJ, 580, 606

Hernquist L., 1990, ApJ, 356, 359

Hogan C. J., 2001, Phys. Rev. D, 64, 063515

Hooper D., Serpico P. D., 2007, Journal of Cosmology and Astro-Particle Physics, 6, 13

Ibata R., Lewis G. F., Irwin M., Totten E., Quinn T., 2001, ApJ, 551, 294

Jungman G., Kamionkowski M., Griest K., 1996, Phys. Rep., 267, 195

Kahn F. D., Woltjer L., 1959, ApJ, 130, 705
Kandrup H. E., Sideris I. V., 2002, Celestial Mechanics and Dynamical Astronomy, 82, 61
Kandrup H. E., Sideris I. V., 2003, ApJ, 585, 244
Kandrup H. E., Siopis C., 2003, MNRAS, 345, 727
Laskar J., 1988, A&A, 198, 341
Laskar J., 1990, Icarus, 88, 266
Laskar J., 2003, arXiv:math/0305364
Lichtenberg A., Lieberman M., 1983, Regular and Stochastic Motion. Springer, New York, Heidelberg, Berlin
Lynden-Bell D., 1962, MNRAS, 124, 95
Merritt D., 1996, AJ, 111, 2462
Merritt D., Fridman T., 1996, ApJ, 460, 136
Merritt D., Valluri M., 1996, ApJ, 471, 82
Merritt D., Valluri M., 1999, AJ, 118, 1177
Miller R. H., 1964, ApJ, 140, 250
Mohayaee R., Shandarin S., Silk J., 2007, Journal of Cosmology and Astro-Particle Physics, 5, 15
Mohayaee R., Shandarin S. F., 2006, MNRAS, 366, 1217
Natarajan A., 2007, Phys. Rev. D, 75, 123514
Natarajan A., Sikivie P., 2005, Phys. Rev. D, 72, 083513
Natarajan A., Sikivie P., 2006, Phys. Rev. D, 73, 023510
Ostriker J. P., Peebles P. J. E., Yahil A., 1974, ApJ, 193, L1
Papaphilippou Y., Laskar J., 1996, A&A, 307, 427
Papaphilippou Y., Laskar J., 1998, A&A, 329, 451
Peccei R. D., Quinn H. R., 1977, Physical Review Letters, 38, 1440
Peebles P. J. E., 1982, ApJ, 263, L1
Pieri L., Branchini E., 2005, Journal of Cosmology and Astro-Particle Physics, 5, 7
Press W. H., Teukolsky S. A., Vetterling W. T., Flannery B. P., 1992, Numerical Recipes in C: The Art of Scientific Computing. Cambridge University Press, New York, NY, USA
Rodionov S. A., Sotnikova N. Y., 2005, Astronomy Reports, 49, 470
Rubin V. C., Ford W. K. J., 1970, ApJ, 159, 379
Rubin V. C., Thonnard N., Ford Jr. W. K., 1980, ApJ, 238, 471
Sanglard V., et al 2005, Phys. Rev. D, 71, 122002
Schnee R. W., 2006, arXiv:astro-ph/0612565
Siegal-Gaskins J. M., Valluri M., 2007, arXiv:astro-ph/0710.0385, 710
Sikivie P., 1998, Physics Letters B, 432, 139
Sikivie P., 1999, Phys. Rev. D, 60, 063501
Sikivie P., Tkachev I. I., Wang Y., 1995, Physical Review Letters, 75, 2911
Smith S., 1936, ApJ, 83, 23
Spooner N. J., 2007, arXiv:astro-ph/0705.3345, 705
Springel V., 2005, MNRAS, 364, 1105
Springel V., Di Matteo T., Hernquist L., 2005, MNRAS, 361, 776
Springel V., Frenk C. S., White S. D. M., 2006, Nat, 440, 1137
Springel V., White S. D. M., Jenkins A., Frenk C. S., Yoshida N., Gao L., Navarro J., Thacker R., Croton D., Helly J., Peacock J. A., Cole S., Thomas P., Couchman H., Evrard A., Colberg J., Pearce F., 2005, Nat, 435, 629
Steigman G., Turner M. S., 1985, Nuclear Physics B, 253, 375
Stiff D., Widrow L. M., Frieman J., 2001, Phys. Rev. D, 64, 083516
Stoehr F., White S. D. M., Springel V., Tormen G., Yoshida N., 2003, MNRAS, 345, 1313
Tremaine S., 1999, MNRAS, 307, 877
Valluri M., Merritt D., 1998, ApJ, 506, 686
Wachlin F. C., Ferraz-Mello S., 1998, MNRAS, 298, 22

Xu G., 1995, ApJS, 98, 355
Zhan H., 2006, ApJ, 639, 617
Zwicky F., 1933, Helvetica Physica Acta, 6, 110